Title
Aerosol-Ice-Cloud Interactions in a Perturbed Parameter Ensemble

Journal
JOURNAL OF CLIMATE, 39(14)

ISSN
0894-8755

Authors
Duran, Brandon M
Lutsko, Nicholas J
Wall, Casey J

Publication Date
2026-07-01

DOI
10.1175/JCLI-D-25-0724.s1

Aerosol-Ice-Cloud Interactions in a Perturbed Parameter Ensemble

Brandon M. Duran, [a] Nicholas J. Lutsko, [a] and Casey J. Wall [b,c]

[a] *Scripps Institution of Oceanography, University of California at San Diego, La Jolla, CA, USA*
[b] *Department of Meteorology, Stockholm University, Stockholm, Sweden*
[c] *Bolin Center for Climate Research, Stockholm University, Stockholm, Sweden*

ABSTRACT: The effective radiative forcing (ERF) from aerosol-cloud interactions (ERFaci) remains poorly constrained and increases uncertainty in future warming projections. While aerosol effects on liquid clouds have been studied extensively in both models and observations, less attention has been paid to the ERF from aerosol-ice-cloud interactions (ERFaci$_{ice}$). We introduce a new method for isolating the shortwave (SW) ERFaci$_{ice}$ in global climate models (GCMs) using histograms of monthly averaged ice cloud fraction partitioned by ice crystal effective radius (r_e) and ice water path (IWP). Combining the cloud histograms with radiative kernels enables estimation of the total SW ERFaci$_{ice}$, which can be further decomposed into contributions from r_e, IWP, and cloud amount changes. The approach is illustrated with a new perturbed parameter ensemble (PPE) using the Community Atmosphere Model, version 6 (CAM6). The overall cooling effect from SW ERFaci$_{ice}$ is estimated to be -0.43 Wm^{-2} in the ensemble mean, a non-negligible contribution to the total ERFaci. A pathway is proposed that relates aerosol-induced subtropical low cloud changes to tropical ice cloud changes via changes in boundary layer moisture. The PPE results demonstrate that dynamical changes can drive the SW aerosol forcing on ice clouds in certain regions, adding another dimension of complexity to aerosol-cloud interactions.

SIGNIFICANCE STATEMENT: Aerosols can affect Earth's climate through their interactions with clouds, and their effects on ice clouds remain highly uncertain. Here, we develop a standardized approach for quantifying the impact of aerosols on ice clouds in global climate models. We find that ice cloud changes from aerosols have likely cooled the planet, but that adjustments in how a model represents aerosol and cloud processes can lead to very different ice cloud responses. Our work shows that low cloud changes can trigger ice clouds shifts in faraway regions, underscoring the importance of viewing aerosol and cloud interactions through the lens of a coupled system.

1. Introduction

Aerosol-cloud interactions (ACI) have remained highly uncertain despite concerted efforts to understand and quantify them. The IPCC's Sixth Assessment Report estimated an overall cooling from ACI of -1.0 Wm^{-2}, but provided wide bounds on the magnitude of cooling (-1.45 to -0.25 Wm^{-2}, 90% confidence; Forster et al. 2021). The cooling from ACI offsets almost none to over half of the 2.16 Wm^{-2} of warming associated with CO_2. The degree to which cooling from ACI has masked the warming effects of CO_2 has clear implications for the evolution of global temperatures. Stronger aerosol masking would imply more historical cooling from aerosols, hence accelerated warming as aerosol emissions decline in the future, and vice versa. Without better constraints on how much aerosol-cloud interactions have offset the warming effects of greenhouse gases, the uncertainty in our projections of future warming cannot be significantly narrowed.

Efforts to reduce uncertainty in the historical ERFaci have mostly concentrated on aerosol-liquid-cloud interactions. As a result, aerosol-ice-cloud interactions remain understudied despite their potential importance to the planetary radiative balance (Storelvmo 2017). It is known that aerosol impacts on ice clouds are both aerosol-type and nucleation-mode specific. Ice crystals may form through homogeneous freezing of sulfate haze droplets at upper-tropospheric temperatures and high supersaturations (Koop et al. 2000), while mineral dust can serve as an effective ice nucleating particle (INP) for heterogeneous nucleation at lower supersaturations (Cantrell and Heymsfield 2005; Hoose and Möhler 2012). Increases in sulfate from anthropogenic emissions lead to increases in ice crystal number (N_i; Gryspeerdt et al. 2018; Mitchell et al. 2018), implying greater reflectivity. In the shortwave (SW), this enhanced reflectivity can be thought of as a corollary of the Twomey effect (Twomey 1977). However, depending on the particle size and number distributions, increased N_i can enhance longwave (LW) emissivity and act to partially or entirely counteract SW effects (Gryspeerdt et al. 2020). In contrast, perturbations to insoluble INPs, like dust, have impacts that vary as a function of the dominant ice nucleation mode. In a heterogeneous freezing-dominated environment, where N_i is often aerosol-limited, more INPs can increase N_i by providing more particles that induce ice nucleation; conversely, in conditions where homogeneous nucleation is dominant, more INPs can deplete the available supersaturation below the homogeneous freezing threshold by activating at lower supersaturations, decreasing N_i in a

Corresponding author: Brandon Duran, bmduran@ucsd.edu

"negative Twomey effect" (Kärcher and Lohmann 2003; Gryspeerdt et al. 2018; Hawker et al. 2021). The sensitivity of the ice crystal response to the dominant nucleation mode suggests that the sign and magnitude of ERFaci$_{ice}$ may vary depending on the background nucleation balance and base state N_i.

The few global estimates of ERFaci$_{ice}$ from GCMs demonstrate substantial disagreement in both the magnitude and sign of aerosol forcing on ice clouds. It remains difficult to separate the instantaneous forcing (Twomey effect, r_e changes) from macrophysical cloud adjustments (changes in ice water path and cloud amount) that occur on longer timescales, and very few predictions of the latter exist. Past studies have produced a spectrum of estimates for ERFaci$_{ice}$ (e.g., Gettelman et al. 2012; Gryspeerdt et al. 2020; Nishant et al. 2019; Penner et al. 2009), though comparisons are not straightforward due to the variety of GCMs, ice microphysical schemes, and INP species considered across them. This was summed up well by Heyn et al. (2017), who highlighted both the variability in predicted ERFaci$_{ice}$ as well as the lack of CMIP5 GCMs that parameterize aerosol effects on ice clouds. Zelinka et al. (2014, 2023) showed that in CMIP5 and CMIP6, models that do parameterize aerosol-ice-cloud interactions tend to have more-negative SW ERFaci that is partially compensated by more-positive LW ERFaci. However, in-depth analysis of each model's high cloud response to aerosol is limited and suggests varying mechanisms may be at play (see Fig. 8 in Zelinka et al. 2014; Oshima et al. 2020). Developing new model parameterizations is confounded by a lack of INP and ice cloud observations, without which it is impossible to bound the contribution of aerosol-ice-cloud interactions to the total ERFaci.

Addressing the existing uncertainty in SW ERFaci$_{ice}$ thus requires a standardized technique for estimating aerosol effects on ice clouds, especially considering the diversity in how aerosol-ice-cloud interactions are parameterized across GCMs. Furthermore, there is a pressing need to understand which processes contribute the most uncertainty in the total SW ERFaci$_{ice}$, which is facilitated by decomposing the total forcing into instantaneous microphysical changes and rapid cloud adjustments. Reducing uncertainty in the individual physical processes that contribute to SW ERFaci$_{ice}$ can then enable tighter constraints on estimates of historical aerosol forcing.

Here, we modify the recently developed MODIS-based cloud radiative kernel method (MODIS CRK) for liquid clouds (Duran et al. 2025) to quantify aerosol effects on ice clouds in GCMs. The technique enables us to estimate the radiative effects tied to the ice Twomey effect, IWP, and ICF adjustments, yielding insight into how each component contributes to the overall radiative response. A new aerosol- and microphysics-based perturbed parameter ensemble is generated to explore uncertainty in SW ERFaci$_{ice}$ in a GCM with an advanced treatment of aerosol-ice-cloud interactions.

In what follows, we present a new methodology for estimating the total SW ERFaci$_{ice}$ and its decomposition into changes in ice crystal effective radius, ice water path, and ice cloud amount, and introduce the new aerosol and microphysics perturbed parameter ensemble (PPE) that serves as the testbed for our approach (section 2). Next, in section 3, we apply the MODIS CRK method to the new CAM6 PPE, assess the validity of the technique with respect to more established methods, and frame the analysis according to two subsets of the PPE. In section 4, we outline how subtropical low cloud responses to aerosols influence the tropical atmosphere, and connect stability and ascent changes to ice cloud changes over the tropical Pacific. Observationally-constrained estimates of SW ERFaci$_{ice}$ are shown in section 5. Concluding thoughts and implications of our findings are discussed in section 6.

2. Data and methods

a. GCM simulations

We generate a new PPE using the Community Atmosphere Model version 6 (CAM6). Nineteen parameters related to aerosol and microphysics processes are perturbed to produce 162 ensemble members. A control member uses the default parameter values for CAM6, while the remaining 161 ensemble members differ in the 19 parameter values. The control setup of CAM6 is referred to as the default throughout the text. Latin hypercube sampling is used to generate the other 161 parameter sets following the methodology of Eidhammer et al. (2024). The parameters and their ranges are listed in Table C1. The majority of the parameter ranges are left unchanged from Eidhammer et al. (2024), although we extend the ranges of two parameters relating to autoconversion. Only aerosol and microphysics parameters are perturbed to explore the sensitivity of the cloud response to aerosols without considering additional uncertainty from convective parameterizations.

For each set of parameter combinations, a pair of atmosphere-only simulations are run with imposed climatological SST and sea ice cover. The prescribed SST and sea ice cover have an annual cycle but lack interannual variability and represent climatological averages over 2005–2015. Preindustrial (PI) and present-day (PD) simulations are generated and are identical to each other, except for varying aerosol precursors and emissions. Preindustrial aerosol emissions are derived from representative 1850 values used for CMIP6 (Hoesly et al. 2018). The prescribed aerosol emissions in PD represent a climatological average over the 2006–2014 time period. Dust emissions differ between ensemble members, as they are linearly scaled by the parameter *dust_emis_fact* (higher values reduce dust loading).

Horizontal wind (U, V) fields are nudged to Modern-Era Retrospective analysis for Research and Applications, Version 2 (MERRA2; Koster et al. 2015) reanalysis over the 2010–2011 period. 3-hourly reanalysis data are used and a 12-hour relaxation is applied, as recommended for CAM6 (Buchholz and Emmons 2024). Nudging is employed to damp the effects of large-scale variability in the simulations, so we can attribute different cloud responses to the aerosol perturbation alone (Kooperman et al. 2012). Nudging is applied above around 2 km in the simulations because many of our parameters affect meteorological conditions and cloud adjustments within the boundary layer (Regayre et al. 2023). Further details about model configuration can be found in appendix A. Due to the volume of data generated by the PPE, we analyze monthly mean output.

Our method relies on joint histograms that represent ice-topped clouds partitioned by r_e and IWP (Fig. 1a). The histograms are produced by the MODIS satellite instrument simulator component of the COSP satellite simulator package (Bodas-Salcedo et al. 2011; Swales et al. 2018) and are designed to align with observed satellite retrievals (Pincus et al. 2023). The MODIS simulator determines cloud phase by assessing how much liquid and ice independently contribute to the optical thickness between the top of the highest cloud and one optical depth unit below, to best mimic phase classification by the satellite (Wind et al. 2010). Only clouds whose visible extinction over this interval is at least 70% from ice crystals, which are classified as ice, are analyzed. Evidence suggests that GCMs simulate $r_{e,ice}$ larger than the bounds on the observational histograms (Y. Qin, personal communication), so an additional r_e bin is added to the joint histograms (60–90 μm range) to ensure the cloud histograms capture the majority of ice clouds simulated in the model. Over 20% of ice clouds fall in the 60–90 μm range of the histogram in the CAM6 PPE. Prior works (Wall et al. 2023, 2025; Duran et al. 2025) have used the observed or satellite simulator-produced joint histograms to estimate aerosol indirect effects on liquid clouds and cloud feedbacks, but this work demonstrates the first use of the new MODIS r_e–IWP joint histograms.

b. Shortwave cloud radiative kernel

We use the RRTMG radiative model (Clough et al. 2005) to compute shortwave (SW) cloud radiative kernels (CRK) for the MODIS r_e–IWP joint histograms. The kernels represent the SW radiative flux anomaly at the top of the atmosphere (TOA) that would occur due to a 1% increase in ice cloud fraction in a given histogram bin. The r_e and IWP bin edges are 5.0, 10.0, 20.0, 30.0, 40.0, 50.0, 60.0, and 90.0 μm and 0, 20, 50, 100, 200, 400, 1000, and 20000 gm^{-2}, respectively. For the cloudy-sky radiative transfer calculations, the cloud top is fixed at the 250 hPa pressure level. This value is chosen to best match the modal value for ice-topped clouds in the global MODIS observations, and the SW CRK is insensitive to minor changes in the chosen pressure level.

Let R represent the SW radiative flux at the top of the atmosphere, and let C_{pi} be the ice cloud fraction in the r_e bin p and IWP bin i. For a specified latitude, surface albedo, and calendar month, the kernel K measures how anomalies of C_{pi} change R while holding all non-cloud factors fixed:

$$K = \frac{\partial R}{\partial C_{pi}} \tag{1}$$

For each r_e–IWP bin, TOA fluxes are calculated for four synthetic clouds with properties prescribed by each bin corner. The four cloudy-sky flux values are then averaged to produce a representative cloudy-sky value for each bin, which is subtracted from the bin's clear-sky flux to yield the cloud radiative effect for an overcast sky. For the smallest IWP bins, the cloudy-sky flux is equal to the clear-sky flux for the bottom two bin corners (IWP = 0), hence the cloud radiative effect for these two bin corners is zero. Next, the climatological seasonal cycle of clear-sky surface albedo from the PI simulation of each ensemble member is used to linearly interpolate K from latitude-surface-albedo space to latitude-longitude space (Fig. 1b). The interpolation yields a transformed cloud radiative kernel for each PPE member which is a function of calendar month, latitude, longitude, r_e and IWP, with units of Wm^{-2}%$^{-1}$ (Watts per square meter per percentage of cloud fraction). The remaining kernel methodology is identical to that outlined in Duran et al. (2025). A similar process is followed to generate a longwave (LW) cloud radiative kernel that can be used to estimate LW ERFaci$_{ice}$, although that is not the focus of this work.

One source of uncertainty in developing the radiative kernel is the choice of ice crystal shape parameterization. Given that cloud scattering properties are highly dependent on particle size (r_e), the choice of ice crystal shape parameterization can have substantial radiative impacts. The kernel uses the default Fu (1996) parameterization in RRTMG, but the alternative schemes of Ebert and Curry (1992) and Key and Schweiger (1998) are also tested.

Figure C1 demonstrates the impact of ice crystal shape parameterization on the cloud radiative kernel. Generally, the default kernel is less negative than the Ebert and Curry (1992) kernel for all r_e–IWP bins other than the uppermost IWP bins (1000-20000 gm^{-2}; Fig. C1a), whereas it is more negative than the Key and Schweiger (1998) kernel for all histogram bins (Fig. C1b). The Fu (1996) parameterization thus yields a middle-of-the-road estimate of the radiative impacts of ice cloud changes compared to the other two schemes. Additionally, the Fu (1996) parameterization leads to the best agreement between overall SW ERFaci (liquid+ice clouds) from the MODIS CRK method

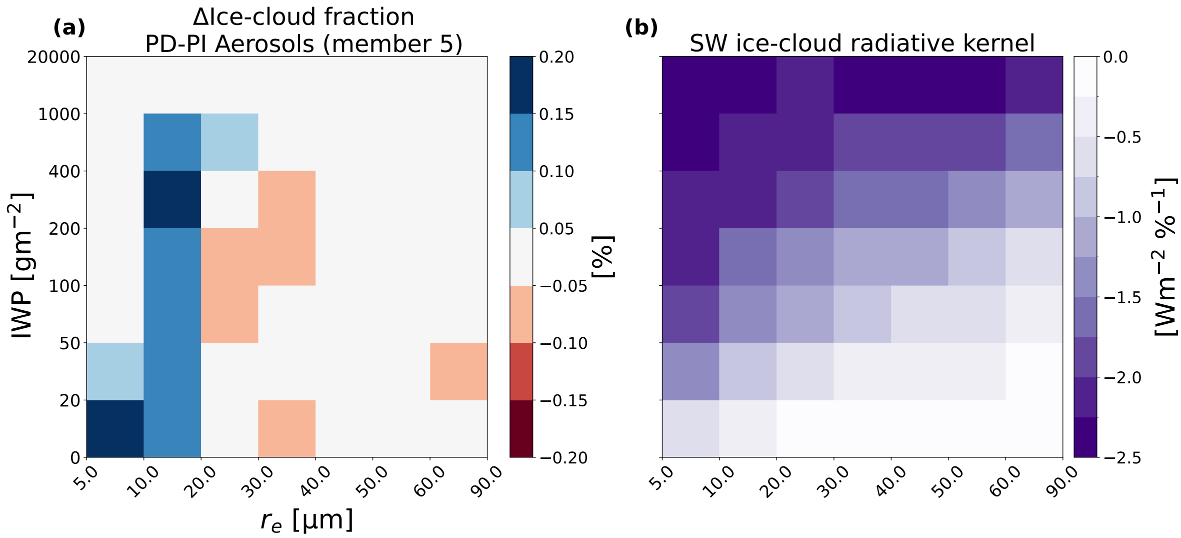

FIG. 1. *Example of the global-mean MODIS ice cloud fraction histogram and radiative kernel.* **(a)** Difference in cloud histograms between the PD and PI simulations for ice-topped clouds in one ensemble member pair. **(b)** SW cloud radiative kernel for ice-topped clouds. The kernel has been interpolated to latitude-longitude space using the preindustrial climatological surface albedo. The cloud histograms and radiative kernels are functions of IWP, r_e, calendar month, latitude, and longitude, but have been spatially and temporally averaged for demonstration purposes.

(Duran et al. 2025) and established methods for estimating the total SW ERFaci, further validating its use.

1) Appropriateness of the SW cloud radiative kernel

We propose to use cloud radiative kernels to diagnose SW ERFaci$_{ice}$, and discuss our reasoning here. While GCMs tend to simulate a net (SW+LW) negative ERFaci from ice clouds as a result of stronger negative SW forcing outcompeting weakly positive LW forcing (Zelinka et al. 2014, 2023), the reason(s) behind this are poorly understood. Approaches for diagnosing ERFaci$_{ice}$ differ in their complexity (Gettelman et al. 2012; Gryspeerdt et al. 2020; Penner et al. 2009) and are not straightforward to compare, further hindering this picture. In contrast, cloud radiative kernels, which rely on a standard definition of cloud and a standard radiative transfer code, provide an appealing approach applicable across different models. Their uniformity enables intermodel differences in ERFaci$_{ice}$ to be directly attributed to different cloud responses. Furthermore, only monthly mean satellite simulator output is required for the kernel approach (Zelinka et al. 2012; Duran et al. 2025). These advantages provide a compelling case for our proposed cloud radiative kernel approach, but additional details warrant attention.

The cloud radiative kernel approach simplifies the diversity of cloud regimes and instead focuses on the radiative effects of clouds based on their gross properties (e.g., r_e, IWP), an issue discussed at length in Zelinka et al. (2016). Ambiguity may be introduced when interpreting the standard MODIS CRK decomposition because the response of a single cloud type in a specific region of r_e–IWP space is considered collectively across the entire cloud population, thus obscuring attribution of the radiative changes. In regions like the deep tropics, where thick deep convective cores and thin anvils coexist, distinct responses in either cloud regime will manifest themselves across the entire r_e–IWP distribution, hindering interpretation. Nevertheless, radiatively, we expect ice clouds with an albedo near 0.5 to exhibit the greatest albedo susceptibility to changes in ice crystal number concentration, and clouds with albedo much greater or less than 0.5 to be less susceptible (Twomey 1991), regardless of their cloud type. The kernel captures this feature by estimating the radiative impacts of changes in r_e with the IWP fixed to its climatological distribution, and vice versa: regions where the cloud climatology is near this optimum albedo will exhibit the highest radiative sensitivity to cloud changes, with the sensitivity falling off with increasing or decreasing cloud albedo. Thus, the main issue of the collective nature of the kernel approach is interpreting the ice cloud response to forcing, not its quantification. The strong agreement between the CRK approach and other methods for estimating SW ERFaci (see Section 4b) further supports the claim that the kernel generates a reasonable first estimate. Separating the MODIS CRK decomposition of ice clouds into thin and thick cloud responses based on IWP (e.g., Gasparini et al. 2019; Sokol et al. 2024; Deutloff et al. 2025; Lutsko et al. 2026) is beyond the scope of this paper but should be the topic of future work.

The advantages of the kernel technique notwithstanding, the emphasis on SW, instead of LW or net, ERFaci is not as clear when examining ice clouds instead of liquid clouds. Located low in the atmosphere, liquid clouds typically have cloud-top temperatures similar to the temperature at the surface, implying a weak impact on LW radiation and motivating the large body of work that examines the SW forcing from aerosol-induced cloud changes. However, unlike liquid clouds, ice clouds can exert significant impacts on outgoing LW radiation due to the temperature contrast between their cool tops and the surface. Therefore, it is unclear whether ERFaci$_{ice}$ is dominated by the SW component of the forcing. Since we are concerned with effective radii changes and subsequent macrophysical cloud adjustments in response to anthropogenic aerosols, the r_e–IWP histograms and kernels are useful for interpreting the different components of aerosol forcing, but the fixed CTP assumption (see Section 2b) required to generate the CRK poses a challenge for diagnosing LW ERFaci$_{ice}$. Assuming a CTP of 250 hPa when generating the LW kernel will lead to an overestimation of the LW cloud radiative effect (CRE) for ice clouds situated below this level in the atmosphere, and underestimate the LWCRE of ice clouds located above this pressure level. While joint histograms of optical depth (τ) and CTP could be used to estimate SW ERFaci$_{ice}$, their interpretability is limited: the radiative impacts of changes in τ could arise from changes in r_e or IWP, or both. Thus, given our focus on aerosol forcing and its components, this work necessarily focuses on SW ERFaci$_{ice}$; details about how the global-mean LW ERFaci$_{ice}$ is estimated are found in Appendix C.

c. SW ERFaci$_{ice}$ decomposition

For each ensemble member, the SW radiative flux anomaly at TOA induced by changes in ice-topped clouds between PD and PI is decomposed into contributions from r_e, IWP, and cloud amount changes. For a specific latitude, longitude, and month, the total ice-cloud-induced SW radiative flux anomaly at TOA, $R^{'}$, is generated by multiplying the cloud radiative kernel K by the change in ice cloud fraction histogram $C^{'}$ and summing over all r_e and IWP bins:

$$R^{'} = \sum_{p=1}^{7}\sum_{i=1}^{7}\left(K_{pi}C^{'}_{pi}\right), \tag{2}$$

where $C^{'}$ represents the change in ice cloud fraction between PD and PI. R' gives an estimate of the contribution of ice-topped clouds to the change in TOA radiation associated with an aerosol perturbation. R' is calculated for each calendar month and then averaged over the full seasonal cycle.

We decompose the right-hand side of Equation 2 to estimate how much r_e, IWP and cloud amount anomalies contribute to $R^{'}$, following Duran et al. (2025). The decomposition is re-derived in appendix B, since the approach is identical, but swaps $r_{e,ice}$ and IWP for $r_{e,liq}$ and LWP. The decomposition of SW ERFaci$_{ice}$ enables the partitioning of ice cloud changes into more physically-interpretable micro- and macrophysical changes.

d. Observations

Observations of cloud properties are taken from the latest MODIS global dataset (Pincus et al. 2023). The raw data are passed through the Collection 6.1 data-processing stream to produce a dataset that facilitates a like-for-like comparison between observations and satellite simulator-derived output from GCMs. Pixelscale observations from Terra (MOD06_L2) and Aqua (MYD06_L2) are combined on daily and monthly timescales to generate the MCD06COSP Level-3 data product (Pincus et al. 2023) used here. Observations from 2002–2024 are used.

Observations of radiative fluxes are taken from the CERES (Clouds and the Earth's Radiant Energy System) satellite Energy Balanced and Filled (EBAF) products (Loeb et al. 2018) version 4.1. Data from 2001-2024 are used, which overlaps with the averaging period for the climatological SSTs (2005-2015) in the model setup.

3. Applying the new MODIS ice CRK method

a. SW ERFaci$_{ice}$ and its components across the PPE

The PPE ensemble mean estimates of the total SW ERFaci$_{ice}$, the ice Twomey effect, and ice cloud adjustments are shown in Figure 2. Global mean values of the total SW ERFaci$_{ice}$ and the three components of the ice MODIS CRK decomposition are compared in Figure 3.

The method estimates an ensemble- and global-mean cooling of -0.43 Wm^{-2} in the SW for ice clouds, which is partially offset by about 35% from LW warming (0.16 Wm^{-2}; see Appendix C for details). There is substantial spread within the PPE (1σ range of 0.75 Wm^{-2}), with over 20% of ensemble members simulating an overall warming in the SW from ERFaci$_{ice}$ (Fig. 3). The default CAM6 setup (-0.25 Wm^{-2}) is close to the ensemble-mean estimate. The total SW ERFaci$_{ice}$ in CAM6 is characterized by a dipole of cooling over Asia that extends into the North Pacific and concentrated warming over the tropical West Pacific (Fig. 2a). A local net warming effect from aerosol-cloud interactions is not seen for liquid clouds in an ensemble of CMIP6 GCMs (Figure 2a; Duran et al. 2025). The warming response in the tropical Pacific is also surprising given the lack of an anthropogenic aerosol signal in the region. The mechanisms behind this response are addressed in section 4.

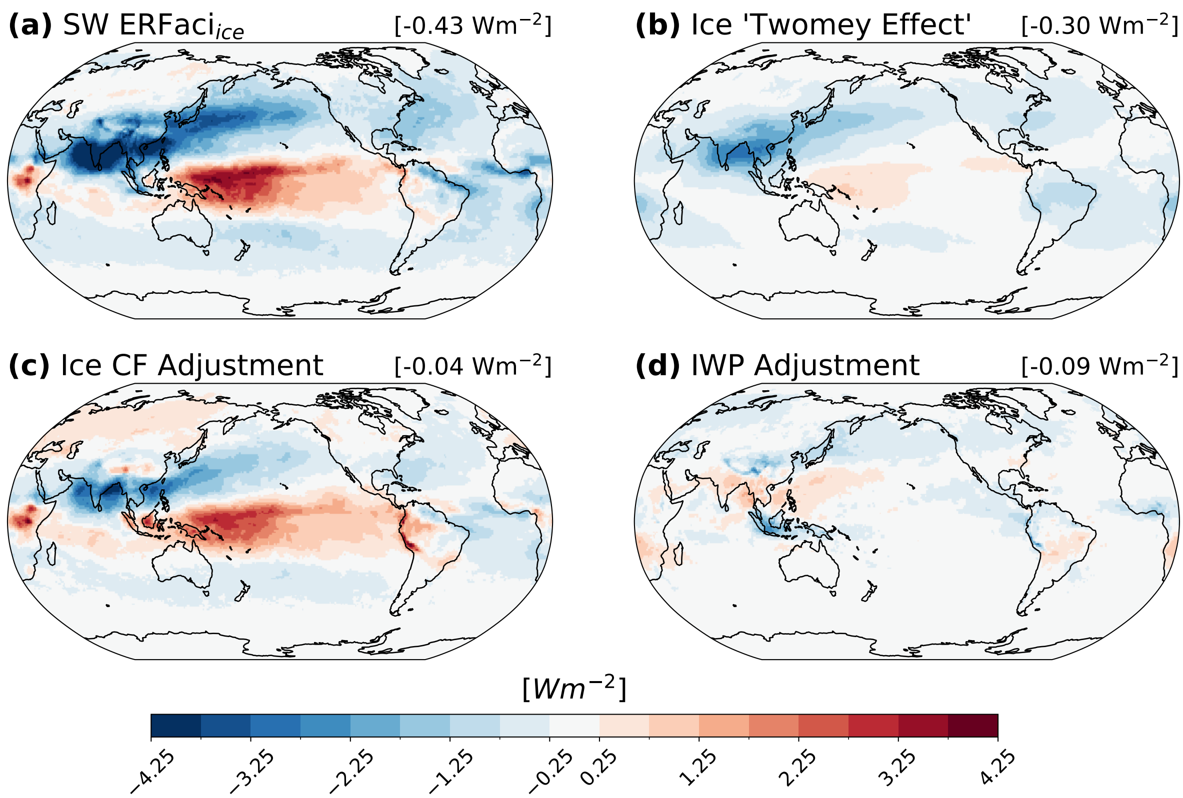

FIG. 2. Ensemble mean SW ERFaci$_{ice}$ and its components. (a) Total SW ERFaci$_{ice}$. Contribution to SW ERFaci$_{ice}$ from the (b) ice Twomey effect, (c) ICF adjustment, and (d) IWP adjustment. Ensemble- and global-mean values of each component are indicated in brackets.

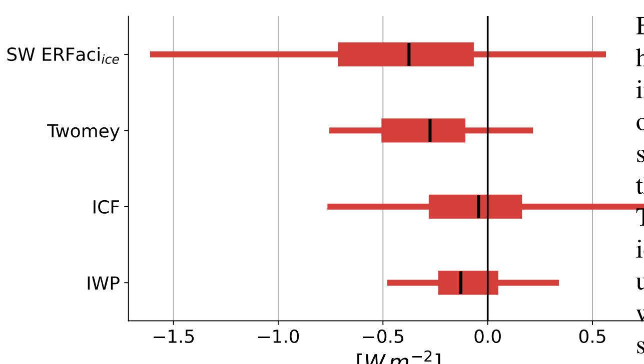

FIG. 3. *Estimates of global-mean SW ERFaci$_{ice}$ and its components across the PPE.* Global-mean estimates of the total SW ERFaci$_{ice}$, ice Twomey effect, ice cloud fraction (ICF) and ice water path (IWP) adjustments. Thin and thick lines represent the 90% and 66% confidence intervals, respectively. The thick vertical line denotes the median value of each quantity.

The ice Twomey effect (Fig. 2b) is the dominant contributor (-0.30 Wm^{-2}) to the overall negative total SW ERFaci$_{ice}$ in the ensemble mean. Its spatial pattern is highly correlated ($r = 0.86$) with the total SW aerosol forcing from ice clouds. The strongest cooling is concentrated over South Asia, where the largest increases in sulfate emissions are present, but to a lesser extent can also be seen off the eastern coasts of North and South America, and Africa. The aerosol perturbation, hence cooling, over North America and Europe is smaller than that over Asia due to the use of climatological emissions from 2006–2014. A small warming signal, indicating increases in effective radius, is seen over the tropical West Pacific, but the shifts in r_e are not large. An overall negative Twomey-like increase in SW ice cloud albedo was also found in five CMIP5 models in Gryspeerdt et al. (2020), although they could not separate r_e changes from IWP adjustments.

The ICF adjustment (Fig. 2c) reflects changes in ice cloud amount, and shows the strongest spatial variability of the three components as well as the most spread (1σ range of 0.52 Wm^{-2}; Fig. 3). Large variations in the high cloud amount in response to aerosol were also found in several AeroCom and CMIP5 models (Gryspeerdt et al. 2020). As with the Twomey effect, it is strongly correlated ($r = 0.89$)

with the total SW ERFaci$_{ice}$. However, in the ensemble mean the SW radiative effects of ice cloud amount changes are near zero (-0.04 Wm^{-2}). It is not immediately obvious why the radiative effects of the cloud amount dipole should approximately balance, which they do in nearly a quarter of ensemble members. Nevertheless, the spatial similarity between Fig. 2b and Fig. 2c suggests that ice cloud amount adjustments are closely tied to microphysical (r_e) changes in the model.

The IWP adjustment (Fig. 2d) is weakly negative (-0.09 Wm^{-2}) across the ensemble, but its spatial pattern differs from the other components and the total SW ERFaci$_{ice}$. The low spatial correlation with the Twomey effect and ICF adjustment indicates that detectable shifts in the IWP distribution of ice clouds occur separately from shifts in r_e and cloud amount (pattern correlation of -0.24 and -0.07, respectively). The IWP adjustment is the strongest component in the default simulation, generating a cooling effect of -0.24 Wm^{-2}. In the global mean, the IWP adjustment tends to be anti-correlated with both the Twomey effect ($r = -0.54$) and ICF adjustment ($r = -0.37$), with little relationship to the total SW ERFaci$_{ice}$ ($r = -0.11$). Due to the relatively weak IWP changes, it is not the focus of our work here.

b. Validation of total SW ERFaci estimates

Having introduced the ensemble mean decomposition of SW ERFaci$_{ice}$, we validate the CRK approach by comparing our estimates of SW ERFaci to other methods. The technique is compared with the widely-used Ghan (2013) and approximate radiative perturbation (APRP) methods (Taylor et al. 2007). Both methods have their own drawbacks: the former relies on specialized aerosol-free diagnostics that are not always output from models and cannot decompose the total SW ERFaci, and the latter cannot partition ACI by cloud-phase nor separate the instantaneous forcing (r_e changes) from the cloud water adjustment. Nevertheless, these methods have been used in numerous studies assessing aerosol forcing across generations of CMIP models (e.g., Zelinka et al. 2014, 2023; Smith et al. 2020).

Direct comparison with these methods is not possible for SW ERFaci$_{ice}$ because both derive estimates of SW ERFaci from all cloud phases. Here, we add the above estimates of SW ERFaci$_{ice}$ to estimates of SW ERFaci$_{liq}$ derived using the approach developed in Duran et al. (2025). While discussing the SW ERFaci$_{liq}$ results in the PPE is beyond the scope of this paper, it is necessary to utilize them here to validate the new method.

The combined liquid+ice MODIS CRK method demonstrates excellent agreement with both the Ghan (2013) and APRP methods in the global mean (Fig. C2a and b). While relying on simulated cloud data from passive satellite retrievals has its own limitations (Zelinka et al. 2025), the strong consistency with common techniques for estimating ERFaci provides support for the use of the MODIS CRK approach, which also confers the benefits of phase-separation and process-based decomposition of ACI. A more thorough examination of spatial differences in estimates of ERFaci is left to a future work.

To further validate the CRK approach, the MODIS SW ERFaci$_{ice}$ estimates are compared to the two-term decomposition of Gryspeerdt et al. (2020). Their decomposition separates SW ERFaci$_{ice}$ into cloud fraction and cloud albedo terms; the former is directly comparable to the ICF adjustment, while the latter is compared to the combined Twomey effect and IWP adjustment. The two techniques demonstrate strong agreement (Fig. C2c and d), further reinforcing the suitability of the MODIS CRK decomposition.

4. Unraveling the drivers of the cloud response

a. Identifying distinct ice cloud changes across the PPE

We seek to understand the drivers of the tropical Pacific-Southeast Asia dipole pattern in Figure 2 by analyzing the most extreme members in the PPE. To this end, we focus on the ten ensemble members with the strongest (COOL) and weakest (WARM) global-mean cooling from SW ERFaci$_{ice}$. While representing the tail ends of the modeled response, the COOL and WARM composites are employed to give the best chance at identifying a plausible systematic driver of the ice cloud response across the PPE, which can be challenging given the amount of parameters perturbed. The results are insensitive to changes in the size of these subsets.

Figure 4a-b show the 10-member composites of total SW ERFaci$_{ice}$ for COOL and WARM, respectively. The COOL group response is an amplified version of the ensemble mean (Fig. 2a), but the WARM group demonstrates a near-opposite response, with slight cooling in the tropical Pacific, and warming over South Asia and other tropical regions. The overall pattern of total SW ERFaci$_{ice}$ in both COOL and WARM is shaped by the ice Twomey effect and ICF adjustment, just as in the ensemble mean. The IWP adjustment is muted except for a large loss in cloud ice over the tropical Pacific in COOL. The large differences in the ice cloud response between COOL and WARM motivates us to investigate the source of this diverging model behavior.

Figure C3 identifies the most distinct parameters between COOL and WARM, as determined by a two-tailed significance test, and Figure 4c demonstrates the two most significant parameters and their relationship to the total SW ERFaci$_{ice}$: micro_mg_autocon_lwp_exp (x-axis) and microp_aero_wsubi_scale (y-axis). Micro_mg_autocon_lwp_exp is the cloud-to-rain autoconversion exponent that modifies the cloud water mass mixing ratio (q_{cl}) in the Khairoutdinov and Kogan (2000)

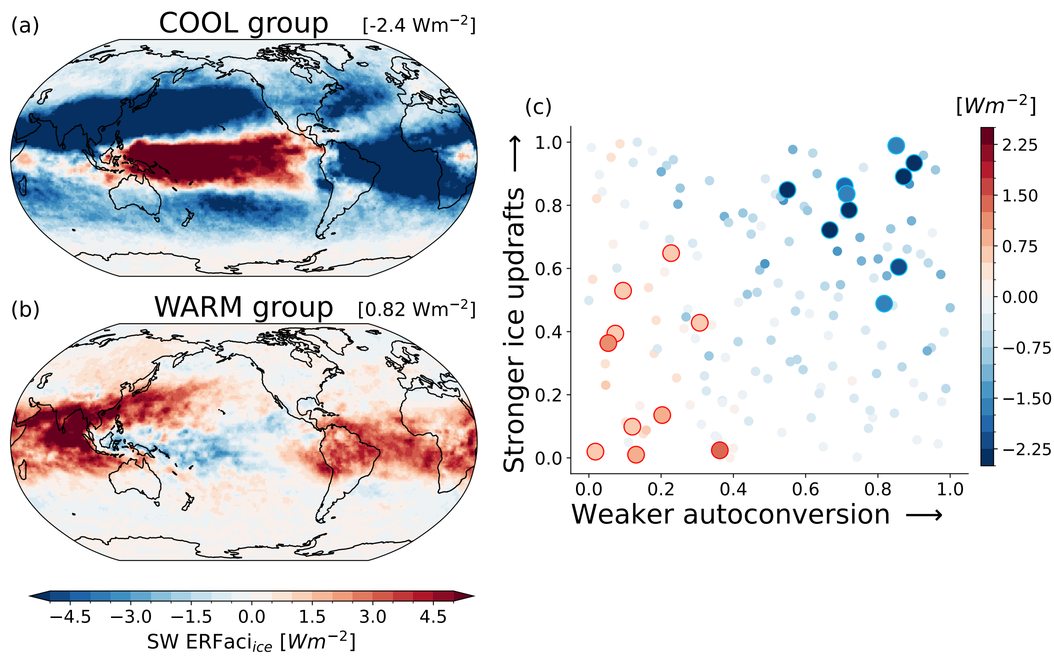

FIG. 4. *Identifying key parameters that drive divergent behavior between COOL and WARM.*. Group-mean total SW ERFaci$_{ice}$ for (a) COOL and (b) WARM. Global-mean values are indicated in brackets in the upper-right corner. (c) Normalized parameter values of micro_mg_autocon_lwp_exp (x-axis) and microp_aero_wsubi_scale (y-axis) across the ensemble. Each dot represents one member. Color shading represents the total SW ERFaci$_{ice}$. COOL and WARM group members are identified by larger points and outlined in blue and red, respectively.

scheme. Higher values correspond to weaker autoconversion rates, hence greater retention of cloud water. Microp_aero_wsubi_scale linearly scales the subgrid vertical velocity passed into the ice nucleation routine. Higher values imply more ice activation, all else being equal.

The COOL group is characterized by weak autoconversion (larger micro_mg_autocon_lwp_exp) and strong ice updrafts (larger microp_aero_wsubi_scale); vice versa for WARM. While it is not surprising that a parameter directly affecting ice nucleation is relevant to SW ERFaci$_{ice}$, it is unclear why a parameter controlling stratiform autoconversion rates defines the COOL and WARM groups. COOL and WARM cloud changes diverge substantially in the tropics, where we would expect micro_mg_autocon_lwp_exp to be of reduced importance. The roles of these parameters in shaping the ice cloud responses to aerosol in the PPE are subsequently investigated.

b. COOL group response

The COOL group response is used to understand the ensemble mean ice cloud response. We focus on the two parameters outlined in section 3a: micro_mg_autocon_lwp_exp and microp_aero_wsubi_scale. The extensive emphasis on COOL is due to its spatial similarity with the ensemble mean response (Fig. 2a). Moreover, when individual ensemble members are clustered into COOL- and WARM-like subsets based on their spatial pattern of total SW ERFaci$_{ice}$, over 80% (n=130) of simulations fall in the COOL-like group.

Large increases in sulfate from PI to PD dominate the overall ice cloud response in COOL. Figure 5a demonstrates the large contribution of homogeneous nucleation to increases in N_i, which is most pronounced over Asia and the Eastern U.S., where anthropogenic aerosol emissions are highest. The regions of enhanced homogeneous nucleation, chiefly Southeast Asia and South America, are coincident with the regions of strongest cooling from SW ERFaci$_{ice}$ in both COOL (Fig. 4a) and the ensemble-mean (Fig. 2a). The nucleation changes occur despite reduced updraft speeds in these regions (Fig. 5c), which alone would weaken homogeneous nucleation. The increased upper-tropospheric sulfate from anthropogenic aerosol emissions overwhelms the muted dynamical changes and greatly enhances homogeneous ice nucleation (Gettelman et al. 2012): we consider these regions to be in an “aerosol-limited” regime in PI.

The tropical Pacific is the sole region in COOL that undergoes substantial decreases in homogeneous nucleation in PD (Fig. 5a). The reduction in homogeneous nucleation occurs despite increases in upper-tropospheric sulfate (not shown), and is collocated with the region of

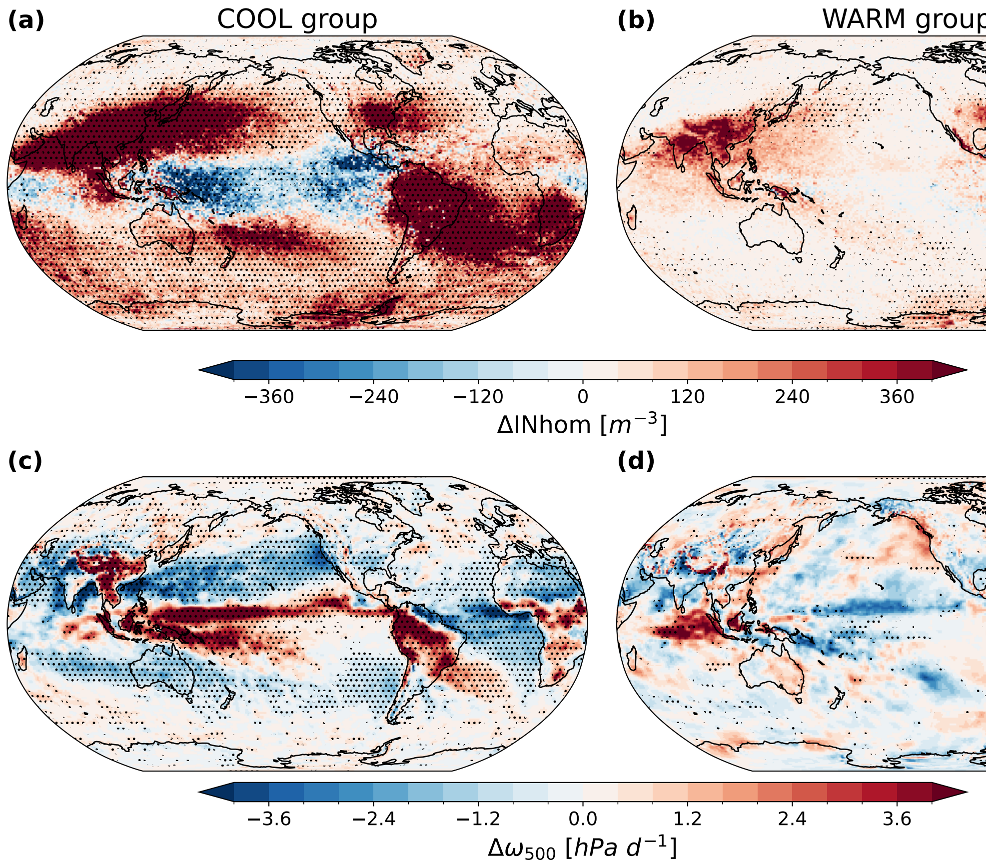

FIG. 5. *Changes in ascent lead ice nucleation changes in tropics.* Change in activated ice number concentration due to homogeneous freezing for (a) COOL and (b) WARM, averaged over model layers between 150 and 250 hPa. Change in vertical pressure velocity at 500 hPa (ω_{500}) for (c) COOL and (d) WARM. (a) and (b) are output from the CAM6 ice nucleation scheme (Liu and Penner 2005; Liu et al. 2007). Statistical significance at the 95% confidence level is stippled.

weakened ascent in the tropical Pacific (Fig. 5c). The pristine conditions of the upper-tropospheric tropical Pacific, as well as the cold temperatures and high updraft speeds that encourage homogeneous nucleation (Kärcher et al. 2006), yield a region where dynamics are not secondary to aerosol changes, even in nudged simulations. These factors all point to a dynamics-driven, rather than aerosol-driven, tropical high cloud response, which we investigate below.

1) CHANGES IN LARGE-SCALE ASCENT AMPLIFIED BY MICROP_AERO_WSUBI_SCALE

To test our hypothesis that tropical Pacific cloud changes are not aerosol driven, we assess the PD aerosol response over this region. We might suspect that increases in sulfate or dust aerosol would help explain ice cloud changes in this region through affecting nucleation processes. As mentioned, a strong weakening of homogeneous nucleation in COOL (≈10-20%, Fig. 5a) is evident at upper levels over the Pacific, coincident with the region of substantial ice cloud loss (Fig. 4a). The weakening of homogeneous nucleation occurs despite increases in sulfate. In the tropical upper-troposphere, coarse mode dust concentrations increase in COOL, which decrease available water vapor, suppress supersaturations, and weaken homogeneous nucleation. By activating at lower supersaturations, the dust changes largely negate increases in sulfate, which alone would strengthen homogeneous nucleation. Nevertheless, decreases in homogeneous nucleation strength are not systematically explained by increased dust loading and enhanced heterogeneous nucleation in PD. In general, dust changes in COOL act to weaken homogeneous nucleation over the tropical Pacific, but they are not the primary driver of ice cloud loss in the region across the PPE.

The weakening of homogeneous nucleation evident in Figure 5a could also be driven by environmental changes. Cooler temperatures and greater relative humidity both would increase the frequency of homogeneous nucleation. The tropical upper troposphere warms and dries in COOL, both of which are unfavorable to homogeneous nucleation. However, these changes are relatively small (percent change < 5) and unlikely to fully explain the nucleation and ice cloud response, but they contribute to the nucleation changes we seek to explain.

Updraft speeds play a pivotal role in the loss of ice clouds over the tropical Pacific in COOL. Faster updrafts create higher supersaturations and enable greater homogeneous freezing (Kärcher and Lohmann 2002). The strong ascending motion in the tropics, coupled with the low temperatures of the tropical upper-troposphere, creates an environment favorable for abundant homogeneous nucleation. In the base state, the effect of microp_aero_wsubi_scale is to either dampen (< 1) or enhance (> 1) homogeneous nucleation by scaling the vertical velocity used for ice nucleation, which is derived from the sub-grid vertical velocity variance associated with turbulent kinetic energy (TKE). Indeed, microp_aero_wsubi_scale closely correlates with the ice number concentration activated via homogeneous freezing in the tropics in PI. Therefore, members of COOL have very active homogeneous nucleation in the tropical upper-troposphere in the base state due to their high values of microp_aero_wsubi_scale.

The scaling of vertical velocity for ice nucleation by microp_aero_wsubi_scale not only sets base state nucleation in the tropics, but also controls the response to aerosol in PD. For values greater than 1, microp_aero_wsubi_scale will intensify the effects of simulated changes in ascent on ice nucleation. This is relevant because large-scale ascent weakens over the tropical Pacific in COOL (Fig. 5c) and in the ensemble mean. Alone, reduced updraft speeds weaken homogeneous nucleation in the upper-troposphere, which occurs in the majority of ensemble members. Microp_aero_wsubi_scale is then responsible for setting the degree to which homogeneous nucleation weakens in response to these slower updrafts. Given their high microp_aero_wsubi_scale values (Fig. 4c), COOL group members show the largest nucleation changes in response to diminished updraft speeds over the tropical Pacific. It is clear that microp_aero_wsubi_scale controls the strength of nucleation changes over the tropical Pacific, but we now seek to understand what drives the weakening of large-scale ascent in the PPE.

2) Subtropical and tropical cloud response linked via boundary layer humidification

We now investigate the mechanisms governing the weakening of large-scale ascent in COOL and seek to connect them to micro_mg_autocon_lwp_exp. This parameter is highly influential in determining the preindustrial base state because it controls the overall cloud-to-rain autoconversion rate, hence it plays a key role in setting the mean cloud state. For example, members with weak autoconversion (high micro_mg_autocon_lwp_exp) have enhanced moisture in the cloud layer in PI due to greater retention of cloud water, whereas members with strong autoconversion quickly rain out cloud water, resulting in small amounts of low clouds globally.

Similar to microp_aero_wsubi_scale, micro_mg_autocon_lwp_exp is relevant for setting both the base state and the response to the aerosol perturbation. With the addition of aerosol, which slows down autoconversion by increasing N_d, thus prolonging cloud lifetime, we would expect stronger increases in cloud water in members with weaker autoconversion. Figure 6 confirms this intuition: changes in subtropical boundary layer (BL) specific humidity are more pronounced in COOL, notably off the western coasts of continents. In contrast, BL moisture changes in WARM are muted, with the aerosol-induced enhancement of cloud water insufficient in overcoming the strong autoconversion set by low values of micro_mg_autocon_lwp_exp. The subtropical regions with large near-surface moisture increases in COOL are characterized by extensive low cloud cover; therefore, we'd anticipate observing the strongest effects of precipitation suppression from aerosols there. But how does this connect to the deep tropics?

Increases in subtropical boundary layer specific humidity in COOL are advected to the deep tropics, leading to a buildup of BL moisture in the tropical West Pacific (Fig. 7a). While fixed-SSTs provide a boundary condition on lower-level temperature and potential temperature (ΔT_{BL}, $\Delta\theta_{BL} \approx 0$), the moisture buildup causes an increase in BL equivalent potential temperature (θ_e; Fig. 7b). θ_e accounts for moisture changes by considering the additional latent heat released by condensing all the moisture in the parcel. It is relevant in the deep convecting regions of the tropics where the atmosphere closely follows a moist adiabat whose profile is tied to the moisture content in the boundary layer (Bretherton et al. 2005; Held and Soden 2006). Therefore, it follows that increases in the boundary layer moisture content in the tropical West Pacific will force the local tropical atmosphere to follow a more stable, warmer moist adiabat (Sokol and Hartmann 2022). Gravity waves then efficiently communicate this perturbed temperature profile imposed by deep convection across the tropics (Bretherton and Smolarkiewicz 1989; Neelin and Held 1987; Pierrehumbert 1995), increasing temperature throughout the free troposphere. Upper-tropospheric static stability increases in response to this adiabatic adjustment (Fig. 7c), suppressing convection and rainfall (Fig. 7d). Stabilization of the tropical atmosphere in response to elevated near-surface moisture explains the weakening of large-scale ascent in COOL (Fig. 5c) and points to a possible pathway by which subtropical low cloud changes can induce changes in tropical high clouds.

Alone, the increase in subtropical near-surface moisture results in greater moisture transport to the Warm Pool region via advection by mean winds; however, this response

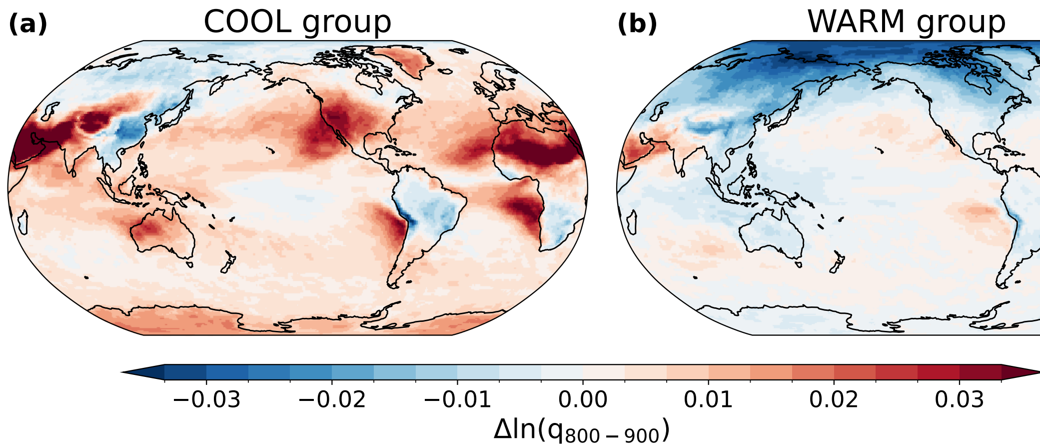

FIG. 6. *Autoconversion parameter mediates boundary layer moisture response.* Fractional changes in boundary layer specific humidity in (a) COOL and (b) WARM. Average over model layers between 800 and 900 hPa.

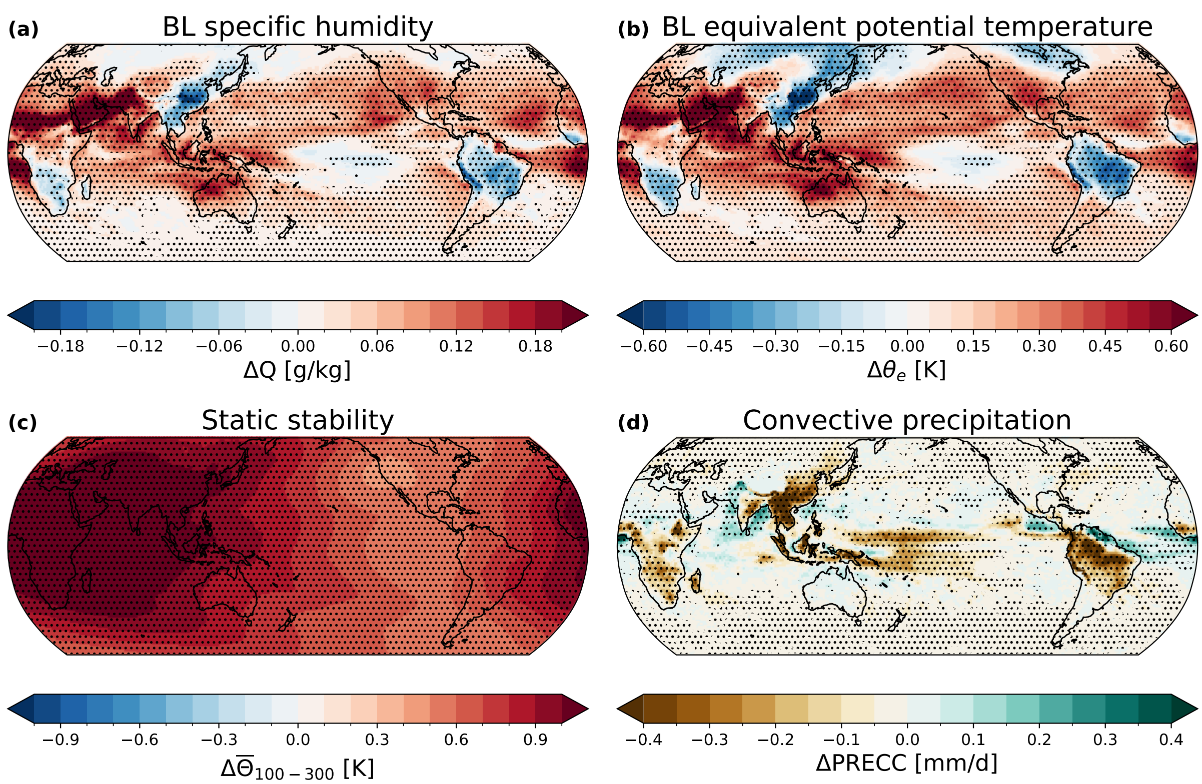

FIG. 7. *Proposed pathway by which subtropical low clouds induce a remote response of the tropical atmosphere.* COOL group-mean PD-PI changes in (a) boundary layer specific humidity (Q), (b) boundary layer equivalent potential temperature (θ_e), (c) upper-tropospheric static stability, and (d) convective precipitation. (a) and (b) are averages over model layers between 800 and 900 hPa. Statistical significance at the 95% confidence level is stippled.

is obscured by the dynamic response, whereby weakening trade winds deliver less moisture to the tropical Pacific. Weakening of low level winds is permitted to evolve in the model because nudging is not applied within the boundary layer. To square our results, we use a moisture balance argument (Betts 1998; Held and Soden 2006;

Williams and Jeevanjee 2025). The initial increase in q_{BL} in the subtropics is advected along climatological winds to the deep tropics and induces stabilization of the tropical atmosphere through a moist adiabatic adjustment. The perturbed tropical temperature profile is more stable and results in weakened ascent over the equatorial Pacific, as well as weakened subsidence over the subtropical North Pacific (Fig. 5c). The slowdown of the overturning circulation triggered by the initial increase in moisture advection from the subtropics to the tropics weakens NH trade winds, resulting in a decrease in moisture convergence in the west Pacific. However, the decreased moisture convergence is outweighed by the strong reductions in ascent, which sequester moisture in the BL more effectively, as shown by the vertical dipole in specific humidity over the Warm Pool region (Fig. 8c). The close correspondence of tropical precipitation changes with competing near-surface moisture and ascent changes confirms that the latter dictate the overall response and are most evident in COOL (Fig. 8a and b).

These results depart from prior work on the connection between subtropical cloud responses to aerosol and circulation changes in the tropics. Large-eddy simulations (LES) with idealized aerosol forcing show an increase in tropical precipitation and associated strengthening of the overturning Hadley circulation in response to subtropical aerosols (e.g., Dagan and Chemke 2016; Dagan et al. 2023; Yamaguchi et al. 2026; Sokol and Wright 2026). The PPE and idealized simulations agree that higher subtropical aerosol loading suppresses local precipitation and enhances moisture flux to the tropics. However, in these studies, tropical precipitation increases with this near-surface moistening, resulting in more latent heat release that amplifies the overturning circulation, and changes in stability are less important. Nevertheless, other studies find that changes in static stability play an important role in the observed weakening of the NH Hadley Circulation (Hess and Chemke 2024), supporting the stability-induced circulation pathway presented.

Through nudging, adjustments in tropical ascent are restricted; therefore, the circulation response is most sensitive to the strengthening of upper-tropospheric stability. Nevertheless, the discrepancy with prior work outlines the challenges associated with using nudging to diagnose ACI, given how it inhibits circulation adjustments, although LES studies are not without their own issues (Abbott and Cronin 2021; Dagan et al. 2022; Anber et al. 2019). Future work should address whether the effect of the stability-induced circulation adjustments shown here is present in free-running simulations. Some ensemble members in the free-running CAM6 PPE (Eidhammer et al. 2024) show similar ice cloud loss in the tropical Pacific; this is discussed in section 6.

3) Tropical high cloud response to circulation and nucleation changes

Thus far, we have demonstrated how two key parameters in the PPE drive the atmospheric response in the tropics through amplification of ascent changes and enhanced boundary layer moisture. Now, we link stability and ice nucleation changes to the reduction of high clouds over the tropical Pacific in COOL.

Decreases in homogeneous freezing as a result of weakened ascent lead to microphysical changes that impact cloud formation and lifetime. A reduction in ice crystal number (N_i) and corresponding increase in ice crystal effective radius are evident in response to weakened homogeneous nucleation (Fig. 9a-b). A shift to fewer, larger ice crystals increases sedimentation velocities, leading to a loss of cloud ice (Fig. 9c) and shorter cloud lifetimes. As a result, ice cloud fraction decreases substantially over the tropical Pacific (Fig. 9d).

The nucleation-driven cloud changes explain the strong warming response in SW ERFaci$_{ice}$ over the tropical Pacific seen in COOL (Fig. 4a) and in the ensemble mean (Fig. 2a). Figure 9 highlights how the tropical Pacific changes in N_i and r_e are relatively small compared to their changes outside the tropics. This is likely due to them being driven by dynamical changes, which are small when evaluated against the strong anthropogenic aerosol perturbation elsewhere. Large decreases in ice crystal size due to anthropogenic aerosols in the extratropics, especially over Southeast Asia, outcompete small tropical r_e increases to drive the overall cooling response of the ice Twomey effect (Fig. 2b). Conversely, tropical ice cloud loss driven by the slowdown of the overturning circulation is substantial enough to balance ice cloud gain over industrialized regions and produce a radiatively-neutral ICF adjustment (Fig. 2c). The associated tropical high cloud changes are important for SW ERFaci$_{ice}$, demonstrating the significance of considering the effects of both aerosol- and dynamics-driven cloud responses.

c. WARM group response

A small proportion (<20%) of the PPE exhibits a qualitatively different ice cloud response from the ensemble mean. The WARM group members display small increases in ice cloud over the tropical Pacific and large ice cloud loss centered over the tropical Indian Ocean. Ice cloud loss can also be seen over much of the tropics outside of the Pacific basin and extending eastward from East Asia (Fig. 4b). Just as in COOL, weakening of ascent is responsible for ice cloud loss in the tropics, but in WARM the ascent changes are confined to the Indian basin (Fig. 5d). We argue that base state aerosol burdens help explain these differences, but do not to focus in-depth on the WARM response because few ensemble members display this behavior and those that do have unrealistically high ice- and low liquid-cloud fraction.

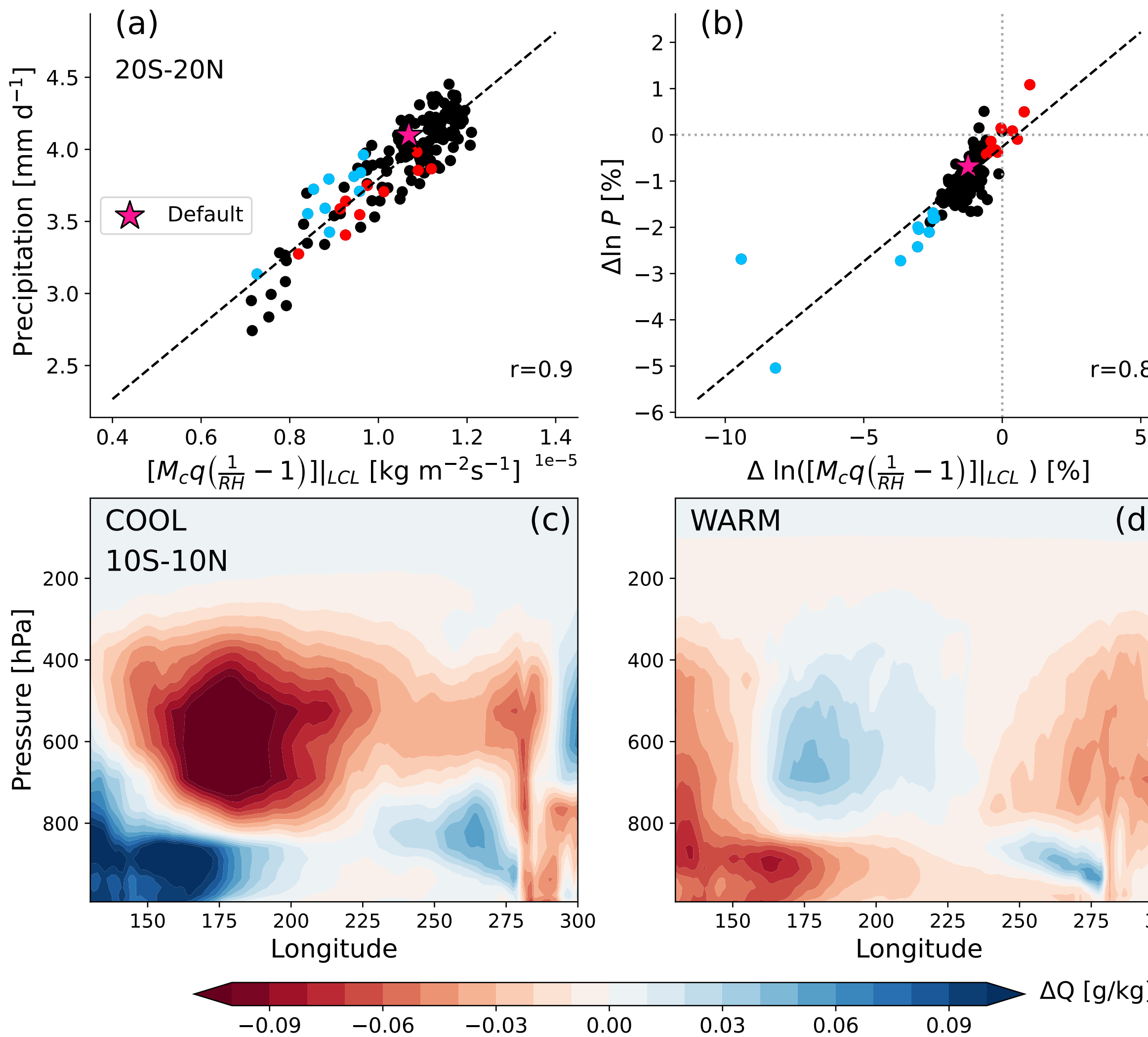

FIG. 8. *Tug of war: moisture budget constraints inform competing q_{BL} and ascent changes.* (a) Preindustrial and (b) PI-to-PD fractional change net flux of WV out of the boundary layer (x-axis) versus tropical precipitation (y-axis). Quantities represent the right and left hand side of Equation 14 in Williams and Jeevanjee (2025) and express a horizontally-averaged water vapor budget. Deep convective mass fluxes from the Zhang and McFarlane (1995) scheme are used for M_c. Blue and red points show the COOL and WARM members. Results averaged over 800-950 hPa. Change in tropical (10°S-10°N, 130-300°E) water vapor in (c) COOL and (d) WARM.

WARM is characterized by stronger dust loading globally in PI (Fig. C4a). The aerosol optical depth (AOD) from dust is almost twice as large in WARM compared to COOL. As a result, base state cloud-top r_e and N_i in the tropics are smaller and larger in WARM, respectively. A peak in N_i is observed just south of India in WARM, about 40° west of the peak in N_i in COOL. This shift in N_i corresponds to a westward-shifted peak in tropical ice cloud fraction and higher IWP over the Indian Ocean. We suspect that dust, an important natural aerosol, is modulating the center of tropical convection in WARM.

Greater dust loading impacts both the base state and the response to the PD aerosol perturbation in WARM. The higher amounts of coarse mode dust enhance heterogeneous nucleation in PI globally, activating at lower supersaturations, hence restricting homogeneous nucleation. As a result, base state homogeneous nucleation over the tropical Pacific is weak and not prone to decreasing dramatically as in COOL, which helps to explain both the lower amounts of ice clouds in this region in the base state, and the lack of cloud changes in PD. Additionally, updrafts strengthen over the tropical Pacific in WARM (Fig. 5d), generating stronger cooling and higher supersaturations favorable to

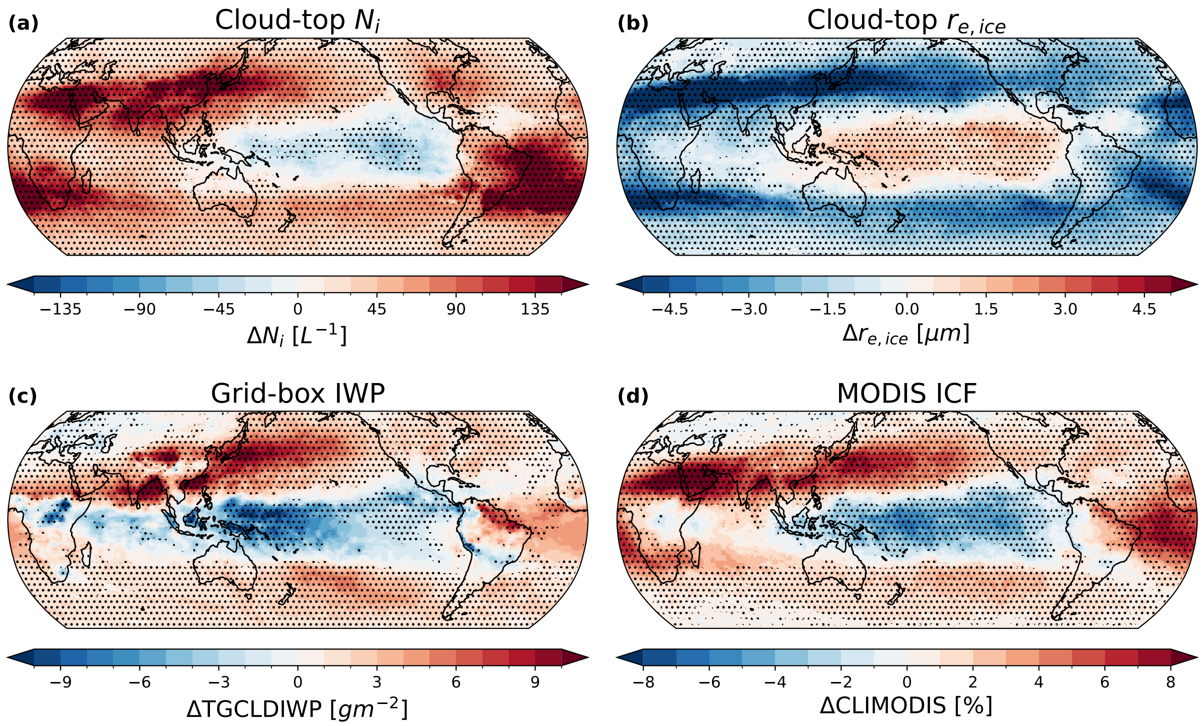

FIG. 9. *Microphysical changes in COOL as a result of changes in ice nucleation.* COOL group-mean PD-PI changes in (a) cloud-top N_i, (b) cloud-top $r_{e,ice}$, (c) grid-box averaged IWP, and (d) MODIS ICF. Statistical significance at the 95% confidence level is stippled.

cloud formation. Outside of this region, we suspect that large increases in sulfate are decoupled from cloud changes because heterogeneous nucleation is sufficiently strong to maintain supersaturations below the homogeneous nucleation threshold.

d. Realistic ensemble members resemble COOL response, but weaker

The mechanisms governing the distinct ice cloud responses across the PPE are evident in the COOL and WARM composites, but may differ in less extreme ensemble members. The majority of ensemble members simulate much more ice cloud than is observed (Fig. 10a), which could suggest the model behavior is not representative of realistic ice cloud responses to aerosol forcing. The consistent overestimation of ice cloud fraction in the PPE may indicate a systematic model bias; we leave this to future work, but suggest that CAM6 may simulate ice clouds that are too low (cloud-top pressure bias) and/or too thick (emissivity bias). Excessive ice cloud fraction was also found in the free-running CAM6 PPE (Song et al. 2024). We turn to subsets of the PPE which best capture the present-day ice cloud state to verify whether the responses outlined above are active in the most realistic climates.

Only 12 and 24 ensemble members fall within the 2σ range (spatiotemporal standard deviation) of observed MODIS ICF and CERES LW cloud forcing, respectively: we dub these subsets the MODIS and CERES groups. Both subsets have strong pattern correlations with the COOL group with respect to SW ERFaci$_{ice}$, albeit with substantially weaker global-mean cooling (-0.21 and -0.45 Wm^{-2}, respectively). The MODIS and CERES groups share weak autoconversion values with COOL, hence they exhibit spatially similar, but weaker, increases in boundary layer moisture in the subtropical stratocumulus regions (pattern correlation of $r = 0.7$ and 0.81 with COOL, respectively). Moreover, the groups share qualitatively similar microphysical responses with COOL, notably the decreases in ice crystal effective radius over Southeast Asia and increases over the tropical Pacific. The microphysical changes are of reduced magnitude compared to COOL due to lower values of microp_aero_wsubi_scale, implying that this parameter acts as an amplifier, rather than a driver, of the typical ice cloud response to aerosol in CAM6. The strong resemblance of both the MODIS and CERES groups with the COOL composite strongly suggests that the proposed atmospheric pathway is active in ensemble members with realistic mean state climates.

5. Using observations to constrain estimates of SW ERFaci$_{ice}$

The parametric uncertainty generated through the PPE leads us to ask whether we can constrain SW ERFaci$_{ice}$. To explore this, observations are leveraged to narrow our ensemble to members that produce realistic ice cloud amounts. By constraining the PPE, we can assess whether the ice cloud response is sensitive to the mean climate state. Since this work is concerned with high cloud changes, ice cloud retrievals from MODIS (ICF) and LW cloud radiative effects (LWCRE) from CERES are used as constraints.

We use a distance function to quantify how closely ensemble members match observations, with added weight given to simulations that best match present-day climate, loosely following Brient and Schneider (2016). Observational constraints are applied to the ensemble to assess how it influences the estimate of SW ERFaci$_{ice}$ in Figure 10b. A normalized Euclidean Distance (ED) is used as the weighting function, such that simulations that best match observations yield more influence on the posterior distribution of SW ERFaci$_{ice}$:

$$\mathrm{ED}_i = \sqrt{\left(\frac{\mathrm{LWCRE}_i - \mathrm{LWCRE}_{\mathrm{CERES}}}{\sigma_{\mathrm{LWCRE}}}\right)^2 + \left(\frac{\mathrm{ICF}_i - \mathrm{ICF}_{\mathrm{MODIS}}}{\sigma_{\mathrm{ICF}}}\right)^2} \tag{3}$$

where $\mathrm{LWCRE_i}$ and $\mathrm{ICF_i}$ are the global-mean values for the i-th ensemble member, $\mathrm{LWCRE_{CERES}}$ and $\mathrm{ICF_{MODIS}}$ are the spatiotemporal means from observations, and σ_{LWCRE} and σ_{ICF} are the PPE ensemble standard deviations of the longwave cloud radiative effect and ice cloud fraction, respectively.

Next, we create weights for each ensemble member using the normalized ED:

$$w_i = e^{-\mathrm{ED}_i} \tag{4}$$

and normalize these weights such that

$$w_i = \frac{w_i}{\sum_i w_i}. \tag{5}$$

The observationally-weighted posterior PDF of SW ERFaci$_{ice}$ (black; Fig. 10b) is narrower than the PPE prior (red; Fig. 10b). The observational constraints reduce the spread in total SW ERFaci$_{ice}$ by 35%, from (-1.05, 0.26) in the prior to (-0.79, 0.05 Wm^{-2}) in the posterior (68% confidence interval), suggesting that aerosol-ice-cloud interactions have an overall cooling effect in the SW over the historical period. The constraints do not strongly affect the central estimate: the mean of the posterior PDF (-0.37 Wm^{-2}) is slightly less negative than the PPE prior (-0.43 Wm^{-2}). We do not show this here, but our constraints strongly support a net (SW+LW) overall cooling from ice clouds, with a 1σ range of (-0.37, -0.12) Wm^{-2}, due to the offsetting nature of SW and LW effects for high clouds.

The constraint based on only two observational metrics is motivated by a desire to evaluate whether estimates of SW ERFaci$_{ice}$ exhibit a base state dependence on ICF in the PPE. However, recent work by Carslaw et al. (2026) and others has highlighted the importance of using a comprehensive set of observations to constrain PPEs. In light of this, we further test the sensitivity of our constraint to three additional observational metrics: MODIS liquid cloud fraction, and CERES SW cloud forcing and net TOA flux. With these five constraints, the central estimate shifts slightly more negative (-0.37 to -0.39 Wm^{-2}) and the spread does not change significantly. Thus, the global-mean constraint on the SW ERFaci$_{ice}$ appears robust. Future work could use a calibrated physics ensemble (CPE; Elsaesser et al. 2025) to test whether SW ERFaci$_{ice}$ can be constrained to a greater degree in an ensemble that produces improved representations of the mean ice cloud state.

6. Conclusions

A new method for isolating aerosol-ice-cloud interactions using MODIS joint histograms of ice-cloud fraction partitioned by r_e–IWP is introduced, extending the work in Duran et al. (2025) beyond liquid clouds. The technique is applied in a new perturbed parameter ensemble, using monthly output to decompose the SW ERFaci from ice clouds into contributions from cloud amount changes and shifts in cloud properties (r_e, IWP). The PPE ensemble mean estimate of SW ERFaci$_{ice}$ (-0.43 Wm^{-2}) contributes to an overall ERFaci estimate (-0.98 Wm^{-2}) that closely aligns with both the central estimate from the IPCC AR6 (-1.0 Wm^{-2}, Forster et al. 2021) and the CMIP6-mean (-0.88 Wm^{-2}, Zelinka et al. 2023). This close correspondence indicates that the PPE is useful for understanding uncertainty in ERFaci, which can be uniquely explored with the MODIS CRK approach and the decomposition of SW ERFaci$_{ice}$ it enables.

In the global mean, the MODIS CRK approach demonstrates strong agreement with prior methods of estimating ERFaci. This further confirms the benefits of the CRK method, which provides added value through decomposing aerosol-induced cloud changes into microphysical changes and cloud adjustments. Future work could examine the spatial differences between the different estimates of ERFaci which, while likely not relevant at the global scale, may have implications for regional forcing. For example, the subtleties of how MODIS classifies clouds influences estimates of ERFaci in certain regions, just as the partitioning of indirect and surface albedo forcing in Ghan (2013) is unreliable in ice-covered regions.

Next, we show the parametric uncertainty in the PPE can produce a spectrum of ice cloud responses to aerosols. The disparate ice cloud changes are traced to variations in two parameters: one controlling ice nucleation rates through

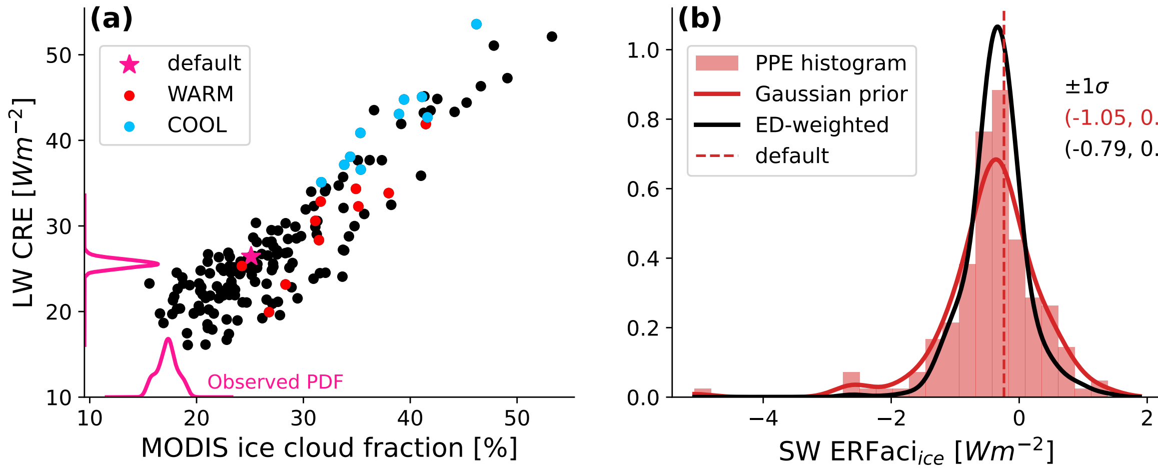

FIG. 10. *Observational constraints reduce uncertainty in SW ERFaci$_{ice}$.* (a) Global-mean MODIS ice cloud fraction (x-axis) and LW cloud radiative effect (y-axis). Each dot represents one member. Default CAM6 simulation is indicated by the pink star. COOL and WARM members are colored red and blue, respectively. Observational PDFs of monthly-mean ICF and LWCRE from MODIS and CERES are shown in pink on the x- and y-axis, respectively. (b) The PDF of SW ERFaci$_{ice}$ from the PPE (shaded histogram), the PPE prior (red), and the observationally-constrained posterior (black). The default CAM6 value is indicated by the vertical dashed red line. Gaussian kernel density estimates are calculated with the scipy.stats.gaussian_kde function (Virtanen et al. 2020). 1σ ranges for the PPE (red) and observationally-constrained (black) PDFs of SW ERFaci$_{ice}$ are listed in the upper-right corner.

scaling vertical velocities (microp_aero_wsubi_scale), and one that influences the cloud-to-rain autoconversion rate (micro_mg_autocon_lwp_exp). High cloud loss in the tropical Pacific is tied to a slowdown in large-scale ascent, which is amplified by microp_aero_wsubi_scale in COOL and substantially weakens homogeneous nucleation. We argue that the weakened tropical ascent is due to the remote influence of the low cloud response to enhanced aerosol loading in the subtropics, which humidifies the boundary layer through precipitation suppression. The advection of BL moisture from the subtropics increases $\theta_{e,BL}$ in the deep tropics and forces an adjustment to a warmer moist adiabat that stabilizes the tropical atmosphere and inhibits ascent and convection. Despite the many parameters perturbed, the majority of the ensemble (> 80%) display this response of cloud loss in the tropical Pacific.

We propose that base state differences in aerosol loading are responsible for driving the contrasting cloud changes in WARM. Weakening of ascent appears responsible for reductions in tropical ice clouds, but in WARM these changes are confined to the Indian Ocean, where the peak in tropical ICF is located. Ice clouds decrease in WARM even over Southeast Asia and its outflows, where sulfate increases are strong, likely due to a combination of strong heterogeneous nucleation and low values of microp_aero_wsubi_scale. The base state differences in WARM, and corresponding differences in SW ERFaci$_{ice}$, provide more evidence that ice cloud responses to aerosol may be sensitive to the dominant nucleation mode (Penner et al. 2018). This sensitivity may become more pronounced as models incorporate the effects of subgrid-scale orographic gravity wave temperature perturbations (Lyu et al. 2023; Tully et al. 2021; Weimer et al. 2023; Yook et al. 2025), as well as more advanced treatments of convective microphysics (Song et al. 2025), both of which influence the mean background microphysical state.

MODIS and CERES observations are applied to our ensemble to reduce spread in the estimate of SW ERFaci$_{ice}$. When ensemble members that best capture present-day ice cloudiness are given more weight, the model evidence strongly suggests that SW ERFaci$_{ice}$ is negative, and the spread in the forcing is reduced by over 30%. The central estimate of SW ERFaci$_{ice}$ is largely insensitive to these constraints (-0.43 to -0.37 Wm^{-2}, unconstrained to constrained) and remains close to the CAM6 default (-0.24 Wm^{-2}). There is even stronger support for a negative net (SW+LW) ERFaci$_{ice}$, due to greater negative SW forcing outpacing more positive LW forcing, in line with Gryspeerdt et al. (2020). These results should be further tested in other models, as the PPE produces too much ice cloud, and variations in LWCRE among members with realistic ICF suggest CAM6 often simulates high clouds that are too thin, but the insensitivity of the constraint to additional observational constraints is promising.

Scarce prior analysis of aerosol-ice-cloud interactions prohibits generalization of our results. However, the simulated SW cooling from aerosol-ice-cloud interactions found here contextualizes why the CMIP6 models that parameterized aerosol effects on ice clouds have stronger-than-average SW ERFaci (see Table 2 in Zelinka et al. 2023). Each of these models differs in what aerosol species it considers as INPs, which prevents us from drawing further conclusions; for instance, MRI-ESM2.0 demonstrates a strong SW cooling from ice clouds over the tropical Indian Ocean, but this is largely driven by the effects of black carbon, which are not included in our study (Fig. 3 in Oshima et al. 2020). This illustrates the difficulty in accurately assessing the structural uncertainty produced by aerosol-ice-cloud interactions and motivates the adoption of the systematic, model-agnostic approach presented in this work.

Our findings raise questions surrounding the use of nudging in ACI studies. Some prior work has shown that circulation changes differ drastically between nudged and free-running simulations (see Fig. 5 in Johnson et al. 2019), while other studies find that nudging is critical for statistical significance (Kooperman et al. 2012; Zhang et al. 2014) and that nudged and free-running simulations yield comparable results for assessing the impact of INPs on cirrus clouds in an aerosol-climate model (Beer et al. 2024). In the PPE, even small changes in ascent can produce large shifts in ice clouds which can be amplified by aerosol and microphysics parameters, especially in regions with minimal aerosol changes. It is surprising that within a nudging framework, dynamics are at the forefront of the cloud response.

Prior studies employ idealized models (e.g., Dagan and Chemke 2016; Dagan et al. 2023) to argue that subtropical aerosol loading should increase equatorial precipitation and amplify the overturning strength of the Hadley circulation. Here, decreases in precipitation over the central Pacific with higher aerosol loading are simulated, emphasizing the need to investigate aerosol-induced changes to circulation and their subsequent implications for aerosol forcing. There is evidence of free-running CAM6 simulations with boundary layer humidification, weakened ascent over the Pacific, and corresponding ice clouds loss (Fig. C5), which hints at the relevance of our proposed mechanism. To robustly test the pathway presented in this work, comparisons between free-running and nudged simulations could be conducted. Whether SW ERFaci$_{ice}$ is sensitive to the effects of different relaxation timescales or where nudging is applied in the vertical should also be tested.

While some ensemble members from the original CAM6 PPE show fingerprints of the atmospheric pathway discussed here, the ensemble ice cloud response differs between the two ensembles, raising questions about the universality of our findings (Eidhammer et al. 2024). Notably, their PPE perturbed parameters relating to shallow and deep convection, in addition to the aerosol and microphysics parameters perturbed here. Many of these parameters exert substantial influence on the cloud response to warming (Duffy et al. 2024), suppressing the influence of the parameters perturbed in this study. The subtropics-to-tropics pathway hinges on two key parameters, micro_mg_autocon_lwp_exp and microp_aero_wsubi_scale, and their deep tropics-mediated interaction: simultaneously perturbing convective parameters that generate spread in the tropical mean state would likely diminish, or entirely obscure, the parameter interdependencies found here. A targeted, one-at-a-time PPE focusing on a handful of key aerosol, microphysics, and convective parameters that have now been identified in broader PPE studies could be developed to assess the robustness of our findings. A smaller parameter selection would also facilitate an intermodel PPE comparison among GCMs that parameterize aerosol-ice-cloud interactions, which would assess whether low clouds influence the high cloud response to aerosol forcing beyond CAM6.

The COOL v WARM dichotomy and the observational constraints confront us with questions about the CAM6 parameter ranges. In-depth analysis of "plausible" parameter values is left to future work; however, given the critical role of microp_aero_wsubi_scale, we briefly address its range. In both PPE and emulator output (not shown), applying observational constraints on various cloud and radiation metrics favors simulations with low values of microp_aero_wsubi_scale (< 2, upper range is 5). Duffy et al. (2024) found this parameter to be highly correlated with the anomalously strong, positive high-cloud altitude feedback in the original CAM6 PPE, and Watson-Parris (2025) found that lower values of microp_aero_wsubi_scale were most compatible with both energetic and process-based constraints on aerosol forcing. Prior results and inter-PPE comparison strongly suggest that large values of this parameter yield unrealistic high cloud changes that skew both ACI and cloud feedbacks. In future PPEs, the upper range of microp_aero_wsubi_scale should be reduced to assess the influence of other aerosol and microphysics parameters.

This work contributes a previously-unexplored dimension to the existing efforts to constrain our estimates of ERFaci. A standardized technique for estimating the SW ERFaci from ice clouds in GCMs is introduced, and the results indicate an overall cooling in the SW from ice clouds that is partly offset by LW warming. The results provide context to the spread in ERFaci in CMIP6 GCMs that parameterize aerosol-ice-cloud interactions. The MODIS CRK decomposition also suggests that microphysical changes and cloud amount changes are closely coupled in CAM6. We emphasize the need to revisit the ramifications of nudging for ACI studies by demonstrating that ascent changes drive the tropical ice cloud response, even when circulation is constrained. Further work is needed to explore the structural uncertainty in aerosol-ice-cloud interactions among the few CMIP models that parameterize their effects. Subsequent studies should standardize additional forcing details, such as the aerosol species considered as INPs, to facilitate intermodel comparison. A unified approach for assessing the ice cloud response to aerosol would aid our efforts to better constrain the historical effective radiative forcing.

Acknowledgments. The authors are grateful for Duncan Watson-Parris, Ben Mackay, Brian Medeiros, Christina McCluskey, Trude Eidhammer, Ryan Patnaude, Andrew Williams, and Mark Zelinka for insightful discussions and feedback. The authors thank four anonymous reviewers for their comments and suggestions which helped improve the manuscript. BMD would like to thank the xarray (`https://docs.xarray.dev/en/stable/`) and xCDAT (`https://xcdat.readthedocs.io/en/latest/index.html`; Vo et al. 2024) software communities for their public software contributions. BMD is supported by the National Science Foundation Graduate Research Fellowship under Grant No. DGE-2038238. CJW is supported by ERC grant number 101156240 (AC3S). This work is funded by the European Union. Views and opinions expressed are however those of the author(s) only and do not necessarily reflect those of the European Union or the European Research Council Executive Agency. Neither the European Union nor the granting authority can be held responsible for them. The authors would like to acknowledge high-performance computing support from the Derecho system (doi:10.5065/qx9a-pg09) provided by the NSF National Center for Atmospheric Research (NCAR), sponsored by the National Science Foundation.

Data availability statement. MODIS cloud histograms are available from the National Aeronautics and Space Administration (NASA) Level-1 and Atmosphere Archive and Distribution System (`https://doi.org/10.5067/MODIS/MCD06COSP\_M3\_MODIS.062`, NASA (2025)). COSP2 download and installation steps can be found at `https://github.com/CFMIP/COSPv2.0`. Radiative fluxes from CERES are available through the CERES subsetting tool (`https://ceres.larc.nasa.gov/data/`). The original CAM6 PPE output can be found at Eidhammer et al. (2022). Monthly data from the new PPE are available on the NSF NCAR Derecho system. Data to reproduce the figures in the text can be found at Duran (2026). The radiative kernel and code to conduct the decomposition of SW ERFaci$_{ice}$ are available at Duran (2025).

APPENDIX A

GCM description

CAM6 is the atmospheric component of the Community Earth System Model version 2 (Danabasoglu et al. 2020). The Cloud Layers Unified by Binormals (CLUBB; Golaz et al. 2002; Larson 2017) scheme is a high-order closure representation of moist turbulence that unifies the description of the planetary boundary layer, cloud macrophysics, and shallow convection. The microphysical scheme is the two-moment Morrison and Gettelman, version 2 (MG2) scheme, that predicts the mass and number concentration of cloud and precipitation particles (Gettelman et al. 2015). Deep convection is treated by the Zhang and McFarlane (1995) scheme. Ice nucleation is treated according to Liu et al. (2007) and Liu and Penner (2005). In-situ ice nucleation and detrainment from convective clouds are the sources of cloud ice for cirrus. The parameterization represents homogeneous freezing of sulfate aerosols and heterogeneous nucleation on dust, as well as competition between the two nucleation types and the effects of preexisting ice on activation of new ice crystals (Shi et al. 2015). Cirrus N_i is a function of sub-grid updraft velocity, relative humidity, temperature, and sulfate and dust number concentrations (Liu and Penner 2005). Sub-grid vertical velocity variance associated with turbulent kinetic energy (TKE) from CLUBB is utilized by the ice nucleation scheme. Notably, CAM6 does not consider other aerosol species (such as black carbon) for ice nucleation by default. We use tag *cam_cesm2_1_rel_60* with the appropriate modifications for the PPE in order to accommodate the COSP changes needed for the MODIS joint histograms.

APPENDIX B

Derivation of SW ERFaci$_{ice}$

Combining the MODIS joint histograms with our radiative kernels enables us to estimate SW ERFaci$_{ice}$ and its components. We decompose the right-hand side of Eq. (2) to estimate how much r_e, IWP, and cloud-amount anomalies contribute to the total ice-cloud-induced SW radiative flux anomaly at TOA, R'. As noted in the text, the approach is identical to Duran et al. (2025), but focused on ice clouds. First, we decompose the cloud fraction anomaly into two terms. Let C_tot represent the total ice-cloud fraction summed over all histogram bins:

$$C_\mathrm{tot} = \sum_{p=1}^{7}\sum_{i=1}^{7} C_{pi}. \tag{B1}$$

We express the cloud fraction anomaly as

$$C'_{pi} = \frac{\overline{C}_{pi}}{\overline{C}_\mathrm{tot}} C'_\mathrm{tot} + C^*_{pi}, \tag{B2}$$

where overbars indicate values from the climatological seasonal cycle. The first term on the right-hand side of Eq. (B2) represents the contribution to C'_{pi} from a change in cloud cover if C'_tot were distributed across the r_e–IWP bins such that the normalized cloud distribution in r_e–IWP space remains the same as the climatology. This term accounts for the change in total ice-cloud fraction, proportioned according to the climatological distribution (assume no shift in cloud properties, just amount). The second term on the right-hand side captures any anomalies of C_{pi} that remain after removing $(\overline{C}_{pi}/\overline{C}_\mathrm{tot})C'_\mathrm{tot}$; i.e., shifts in the cloud distribution across r_e and IWP, holding total ice-cloud fraction fixed. C^*_{pi} vanishes when summed over all r_e–IWP bins.

Next, we decompose the radiative kernel into two terms:

$$K_{pi} = K_0 + \hat{K}_{pi}. \tag{B3}$$

K_0 is the average of K_{pi} weighted by the climatological cloud fraction,

$$K_0 \equiv \sum_{p=1}^{7}\sum_{i=1}^{7}\left(\frac{\overline{C}_{pi}}{\overline{C}_\mathrm{tot}} K_{pi}\right), \tag{B4}$$

and $\hat{K}_{pi} \equiv K_{pi} - K_0$. Combining the relationships from Eqs. (2)-(B4), the ice-cloud-induced SW flux anomaly at TOA is given by

$$R' \equiv \sum_{p=1}^{7}\sum_{i=1}^{7}(K_{pi}C'_{pi}) = K_0 C'_\mathrm{tot} + \sum_{p=1}^{7}\sum_{i=1}^{7}(\hat{K}_{pi}C^*_{pi}). \tag{B5}$$

$K_0 C'_\mathrm{tot}$ represents the ice-cloud-induced SW flux anomaly at TOA that would occur given a change in total ice-cloud fraction, distributed across the climatological distribution of clouds in the r_e–IWP joint-histogram space. This term is the cloud fraction adjustment, also known as the "proportionate change in cloud fraction" from Zelinka et al. (2012).

Next, we decompose $\hat{K}_{pi}$ into three terms:

$$\hat{K}_{pi} = \hat{K}_p + \hat{K}_i + \hat{K}_\mathrm{res}, \tag{B6}$$

where

$$\hat{K}_p = \sum_{i=1}^{7}\left(\hat{K}_{pi}\sum_{p=1}^{7}\frac{\overline{C}_{pi}}{\overline{C}_\mathrm{tot}}\right), \tag{B7}$$

$$\hat{K}_i = \sum_{p=1}^{7}\left(\hat{K}_{pi}\sum_{i=1}^{7}\frac{\overline{C}_{pi}}{\overline{C}_\mathrm{tot}}\right), \tag{B8}$$

and

$$\hat{K}_\mathrm{res} = \hat{K}_{pi} - \hat{K}_p - \hat{K}_i. \tag{B9}$$

We can then express R' as

$$R' = K_0 C'_{\text{tot}} + \sum_{p=1}^{7}\left(\hat{K}_p \sum_{i=1}^{7} C^*_{pi}\right) + \sum_{i=1}^{7}\left(\hat{K}_i \sum_{p=1}^{7} C^*_{pi}\right) + \sum_{p=1}^{7}\sum_{i=1}^{7}(\hat{K}_{\text{res}} C^*_{pi}) \tag{B10}$$

or

$$R' = R'_{\text{CF}} + R'_{r_\text{e}} + R'_{\text{IWP}} + R'_{\text{res}}. \tag{B11}$$

The first term on the right-hand side of Eqs. (B10) and (B11), R'_{CF} represents the contribution of changes in the total ice-cloud fraction to the SW flux anomaly R'. The second term is generated by multiplying an effective kernel that accounts for variations in r_e by the change in cloud fraction at each r_e bin, and represents the contribution of r_e anomalies to the SW flux anomaly R' with IWP and total ice-cloud fraction held fixed. The third term on the right-hand side of Eqs. (B10) and (B11) is similar to the second, but represents the contribution of IWP anomalies to R' with r_e and total ice-cloud fraction held fixed. These terms are computed from the differences between PD and PI, where SSTs are identical but aerosol emissions differ, hence they represent the ICF adjustment, ice Twomey effect, and IWP adjustment, respectively. Each term is computed with the other properties held fixed, and the last term on the right-hand side (R'_{res}) is the residual of the decomposition. In this way, we are able to capture the distinct roles of changes in different cloud properties to the overall SW ERFaci$_{ice}$.

APPENDIX C

Estimation of LW ERFaci$_{ice}$

MODIS joint histograms of ICF partitioned by optical depth (τ) and cloud-top pressure (CTP) are combined with radiative kernels to estimate LW ERFaci$_{ice}$ in this work (see Sections a and 5). While the r_e–IWP joint histograms can be used to estimate LW ERFaci$_{ice}$, a fixed CTP of 250hPa is assumed when calculating the LW cloudy-sky forcing to generate the kernel. The LW kernel in r_e–IWP space is sensitive to this CTP assumption, given that it determines cloud-top temperature and emission. Thus, the τ–CTP kernel, which does not assume a fixed CTP, is preferred. A decomposition of LW ERFaci$_{ice}$ similar to that for SW ERFaci$_{ice}$ (see Appendix B) can be performed, but is not included here since we rely solely on the total LW ERFaci$_{ice}$. For the τ–CTP decomposition, there is an identical ICF adjustment term, as well as an altitude (CTP changes) and thickness term (τ changes).

The MODIS estimates of LW ERFaci$_{ice}$ are highly correlated (r^2=0.91) with the change in LW cloud radiative effect (LWCRE). We expect the total LW ERFaci to be dominated by ice clouds, since the cloud-top temperatures of liquid clouds are much closer to the surface temperature; hence, LW forcing from warm clouds should be small compared to cold clouds. The strong correspondence between the MODIS estimates and ΔLWCRE in the global-mean support the use of the MODIS CRK approach for computing LW ERFaci$_{ice}$. Further details about the LW kernel and its generation can be found in Wall et al. (2025).

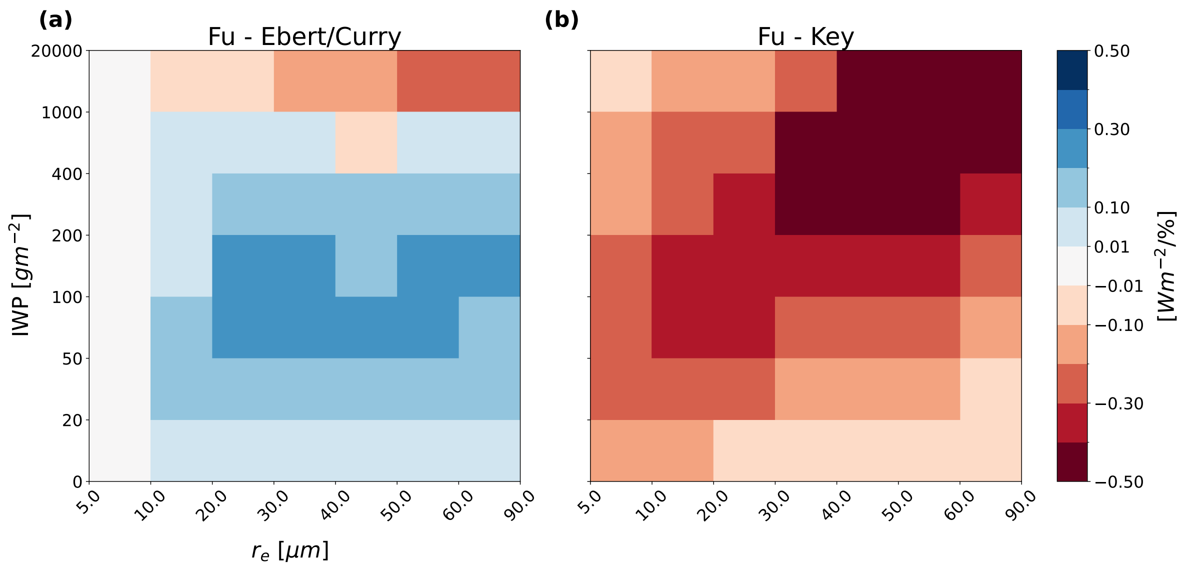

Fig. C1. *SW ice-cloud radiative kernel sensitivity to ice crystal shape parameterization.* Difference between the default Fu (1996) and the (a) Ebert and Curry (1992) and (b) Key and Schweiger (1998) schemes. The ice-cloud radiative kernels are functions of IWP, r_e, calendar month, latitude, and surface albedo, but have been spatially and temporally averaged in the example above for demonstration purposes.

Table C1. A description of the parameters perturbed in the PPE, with their ranges. Asterisks indicate parameters with modified ranges compared to Eidhammer et al. (2024). Daggers indicate new parameters.

Parameter	Description	Default	Min	Max	Units
micro_mg_accre_enhan_fact	Accretion enhancing factor	1	0.1	10	-
micro_mg_autocon_fact	Autoconversion factor	0.01	5e-3	0.2	-
micro_mg_autocon_lwp_exp*	KK2000 LWP exponent	2.47	1.8	3.6	-
micro_mg_autocon_nd_exp*	KK2000 autoconversion factor	-1.1	-2.5	0	-
micro_mg_berg_eff_factor	Bergeron efficiency factor	1	0.1	1	-
micro_mg_dcs	Autoconversion size threshold ice-snow	5e-4	5e-5	1e-3	m
micro_mg_effi_factor	Scale effective radius for optics calculation	1	0.1	2	-
micro_mg_homog_size	Homogeneous freezing ice particle size	2.5e-5	1e-05	2e-4	m
micro_mg_iaccr_factor	Scaling ice/snow accretion	1	0.2	1	-
micro_mg_max_nicons	Max ice number concentration	1e8	1e5	1e10	#/kg
micro_mg_vtrmi_factor	Ice fall speed scaling	1	0.2	5	m/s
seasalt_emis_scale	Seasalt emission scaling factor	1	0.5	2.5	-
microp_aero_npccn_scale	Scale activated liquid number	1	0.33	3	-
microp_aero_wsub_min	Min subgrid velocity for liquid activation	0.2	0	0.5	m/s
microp_aero_wsubi_min	Min subgrid velocity for ice activation	1e-3	0	0.2	m/s
microp_aero_wsub_scale	Subgrid velocity for liquid activation scaling	1	0.1	5	-
microp_aero_wsubi_scale	Subgrid velocity for ice activation scaling	1	0.1	5.	-
dust_emis_fact	Dust emissions scaling factor	0.7	0.1	1.2	-
sol_facti_cloud_borne†	In-cloud scavenging of cloud-borne modal aerosols	1	0.5	1	-

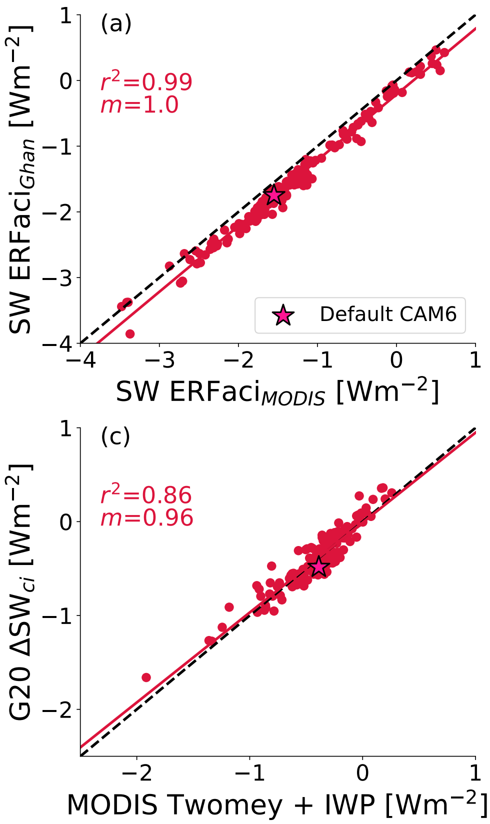

FIG. C2. *Comparing the MODIS CRK estimates of SW ERFaci to established methods.* Global-mean estimates of SW ERFaci derived from the MODIS CRK (x-axis), (a) Ghan (2013), and (b) APRP (y-axes) methods. (c) Estimates of the MODIS Twomey effect and IWP adjustment (x-axis) versus the intrinsic forcing from Gryspeerdt et al. (2020). (d) Estimates of the MODIS ICF adjustment (x-axis) versus the ice cloud albedo term from Gryspeerdt et al. (2020). Each dot is an ensemble member. Dashed black lines represent the one-to-one line. The top left corner indicates the squared coefficient of determination for the ordinary least-squares linear-regression fit (r^2) and the slope of the fit (m). The MODIS CRK method represents the sum of SW ERFaci$_{liq}$ and SW ERFaci$_{ice}$. APRP is calculated following Zelinka (2023).

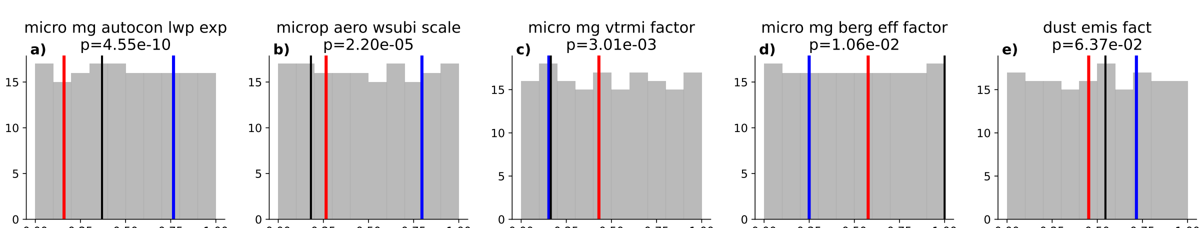

FIG. C3. *Determining parameter differences between COOL and WARM groups.* Histograms of normalized parameter values across the PPE. Default CAM6 parameter value indicated by the vertical black line. COOL and WARM group-mean parameter values indicated by the blue and red vertical lines, respectively. A Welch's t-test is used to determine whether the parameters are significantly different between the COOL and WARM groups. P-values (p) from the t-test are indicated in the title. Parameters not significantly different at the 90% confidence level ($p > 0.1$) are not shown. Parameters are sorted by their significance from left to right (ascending p-value).

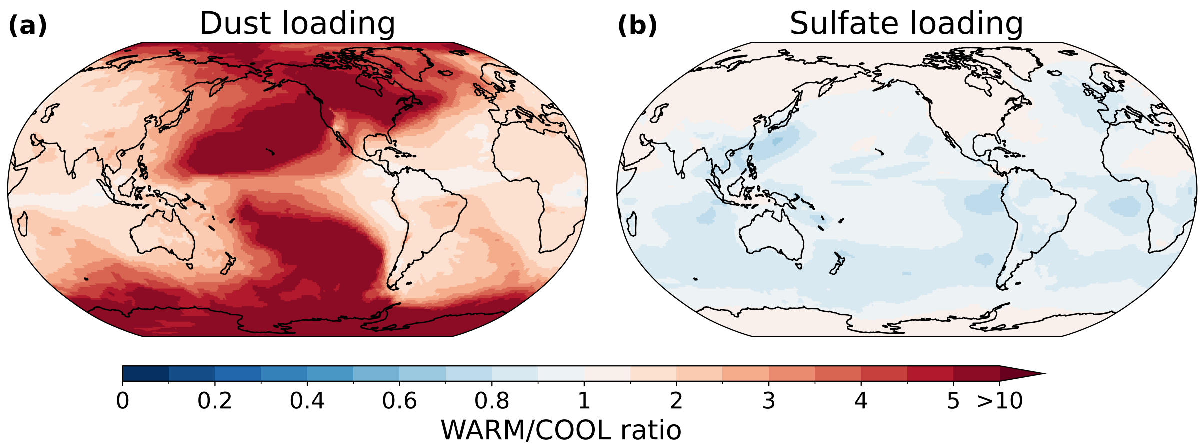

Fig. C4. *Comparing dust and sulfate aerosol burdens between WARM and COOL.* Ratio of WARM-to-COOL (a) dust and (b) aerosol burden in the PI simulation. Aerosol burdens are in units of kgm^{-2}, and the ratio is unitless. Values greater than 1 (red) indicate greater aerosol loading in WARM.

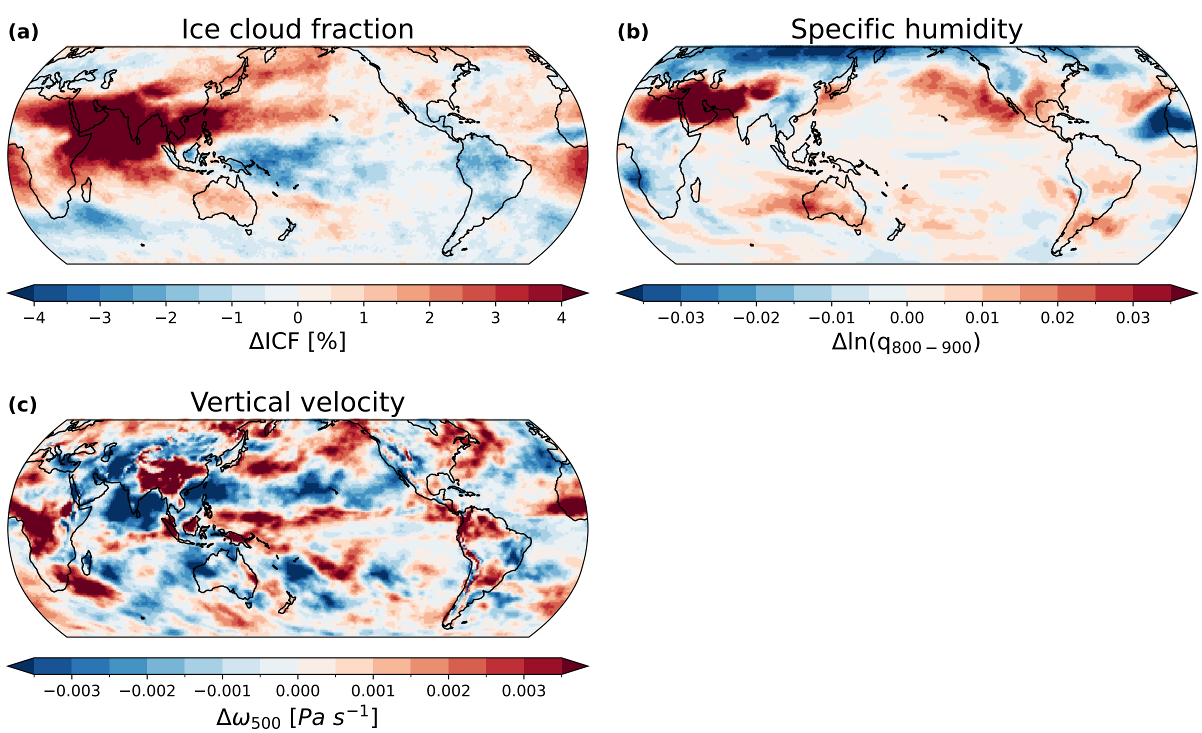

Fig. C5. *Similar ice cloud response in free-running CAM6 simulations.* Change in (a) MODIS ice cloud fraction, (b) boundary layer specific humidity, and (c) vertical pressure velocity from the original CAM6 PPE (Eidhammer et al. 2024). Ensemble members are first ranked by the strength of ice cloud loss in the tropical Pacific (10°S-10°N, 140°-190°E), and then the fifteen members with the strongest reduction of ice cloud in this region are selected. Spatial patterns are robust to changes in the number of members chosen.

References

Abbott, T. H., and T. W. Cronin, 2021: Aerosol invigoration of atmospheric convection through increases in humidity. *Science*, **371 (6524)**, 83–85.

Anber, U. M., S. Wang, P. Gentine, and M. P. Jensen, 2019: Probing the response of tropical deep convection to aerosol perturbations using idealized cloud-resolving simulations with parameterized large-scale dynamics. *Journal of the Atmospheric Sciences*, **76 (9)**, 2885–2897.

Beer, C. G., J. Hendricks, and M. Righi, 2024: Impacts of ice-nucleating particles on cirrus clouds and radiation derived from global model simulations with made3 in emac. *Atmospheric Chemistry and Physics*, **24 (5)**, 3217–3240.

Betts, A. K., 1998: Climate-convection feedbacks: Some further issues. *Climatic Change*, **39 (1)**, 35.

Bodas-Salcedo, A., and Coauthors, 2011: Cosp: Satellite simulation software for model assessment. *Bulletin of the American Meteorological Society*, **92 (8)**, 1023–1043.

Bretherton, C. S., P. N. Blossey, and M. Khairoutdinov, 2005: An energy-balance analysis of deep convective self-aggregation above uniform sst. *Journal of the atmospheric sciences*, **62 (12)**, 4273–4292.

Bretherton, C. S., and P. K. Smolarkiewicz, 1989: Gravity waves, compensating subsidence and detrainment around cumulus clouds. *Journal of Atmospheric Sciences*, **46 (6)**, 740–759.

Brient, F., and T. Schneider, 2016: Constraints on climate sensitivity from space-based measurements of low-cloud reflection. *Journal of Climate*, **29 (16)**, 5821–5835.

Buchholz, R., and L. Emmons, 2024: Meteorology for physics-based nudging. URL https://wiki.ucar.edu/spaces/camchem/pages/452821200/Meteorology+for+physics-based+nudging.

Cantrell, W., and A. Heymsfield, 2005: Production of ice in tropospheric clouds: A review. *Bulletin of the American Meteorological Society*, **86 (6)**, 795–808.

Carslaw, K. S., and Coauthors, 2026: Opinion: The importance and future development of perturbed parameter ensembles in climate and atmospheric science. *Atmospheric Chemistry and Physics*, **26 (7)**, 4651–4667, https://doi.org/10.5194/acp-26-4651-2026.

Clough, S. A., M. W. Shephard, E. J. Mlawer, J. Delamere, M. J. Iacono, K. Cady-Pereira, S. Boukabara, and P. D. Brown, 2005: Atmospheric radiative transfer modeling: A summary of the aer codes. *Journal of Quantitative Spectroscopy and Radiative Transfer*, **91 (2)**, 233–244.

Dagan, G., and R. Chemke, 2016: The effect of subtropical aerosol loading on equatorial precipitation. *Geophysical research letters*, **43 (20)**, 11–048.

Dagan, G., P. Stier, G. Spill, R. Herbert, M. Heikenfeld, S. C. van den Heever, and P. J. Marinescu, 2022: Boundary conditions representation can determine simulated aerosol effects on convective cloud fields. *Communications Earth & Environment*, **3 (1)**, 71.

Dagan, G., N. Yeheskel, and A. I. Williams, 2023: Radiative forcing from aerosol–cloud interactions enhanced by large-scale circulation adjustments. *Nature Geoscience*, **16 (12)**, 1092–1098.

Danabasoglu, G., and Coauthors, 2020: The community earth system model version 2 (cesm2). *Journal of Advances in Modeling Earth Systems*, **12 (2)**, e2019MS001 916.

Deutloff, J., S. A. Buehler, M. Brath, and A. K. Naumann, 2025: Insights on tropical high-cloud radiative effect from a new conceptual model. *Journal of Advances in Modeling Earth Systems*, **17 (2)**, e2024MS004 615.

Duffy, M. L., B. Medeiros, A. Gettelman, and T. Eidhammer, 2024: Perturbing parameters to understand cloud contributions to climate change. *Journal of Climate*, **37 (1)**, 213–227.

Duran, B. M., 2025: modisiceaci. Zenodo [code], https://doi.org/10.5281/zenodo.17544907.

Duran, B. M., 2026: cam6-ice-aci. Zenodo [code], https://doi.org/10.5281/zenodo.18261823.

Duran, B. M., and Coauthors, 2025: A new method for diagnosing effective radiative forcing from aerosol–cloud interactions in climate models. *Atmospheric Chemistry and Physics*, **25 (4)**, 2123–2146.

Ebert, E. E., and J. A. Curry, 1992: A parameterization of ice cloud optical properties for climate models. *Journal of Geophysical Research: Atmospheres*, **97 (D4)**, 3831–3836.

Eidhammer, T., A. Gettelman, and K. Thayer-Calder, 2022: CESM2.2 CAM6 PPE. NSF National Center for Atmospheric Research, Boulder, CO, https://doi.org/10.26024/bzne-yf09.

Eidhammer, T., and Coauthors, 2024: An extensible perturbed parameter ensemble (ppe) for the community atmosphere model version 6. *EGUsphere*, **2024**, 1–27.

Elsaesser, G. S., and Coauthors, 2025: Using machine learning to generate a giss modele calibrated physics ensemble (cpe). *Journal of Advances in Modeling Earth Systems*, **17 (4)**, e2024MS004 713.

Forster, P., and Coauthors, 2021: The Earth's energy budget, climate feedbacks, and climate sensitivity. *Climate Change 2021 – The Physical Science Basis: Working Group I Contribution to the Sixth Assessment Report of the Intergovernmental Panel on Climate Change*, V. Masson-Delmotte, P. Zhai, A. Pirani, S. L. Connors, C. Péan, S. Berger, N. Caud, Y. Chen, L. Goldfarb, M. I. Gomis, M. Huang, K. Leitzell, E. Lonnoy, J. B. R. Matthews, T. K. Maycock, T. Waterfield, O. Yelekçi, R. Yu, and B. Zhou, Eds., Cambridge University Press, 923–1054, https://doi.org/10.1017/9781009157896.009.

Fu, Q., 1996: An accurate parameterization of the solar radiative properties of cirrus clouds for climate models. *Journal of climate*, **9 (9)**, 2058–2082.

Gasparini, B., P. N. Blossey, D. L. Hartmann, G. Lin, and J. Fan, 2019: What drives the life cycle of tropical anvil clouds? *Journal of Advances in Modeling Earth Systems*, **11 (8)**, 2586–2605.

Gettelman, A., X. Liu, D. Barahona, U. Lohmann, and C. Chen, 2012: Climate impacts of ice nucleation. *Journal of geophysical research: Atmospheres*, **117 (D20)**.

Gettelman, A., H. Morrison, S. Santos, P. Bogenschutz, and P. Caldwell, 2015: Advanced two-moment bulk microphysics for global models. part ii: Global model solutions and aerosol–cloud interactions. *Journal of Climate*, **28 (3)**, 1288–1307.

Ghan, S. J., 2013: Estimating aerosol effects on cloud radiative forcing. *Atmospheric Chemistry and Physics*, **13 (19)**, 9971–9974.

Golaz, J.-C., V. E. Larson, and W. R. Cotton, 2002: A pdf-based model for boundary layer clouds. part i: Method and model description. *Journal of the atmospheric sciences*, **59 (24)**, 3540–3551.

Gryspeerdt, E., O. Sourdeval, J. Quaas, J. Delanoë, M. Krämer, and P. Kühne, 2018: Ice crystal number concentration estimates from lidar–radar satellite remote sensing–part 2: Controls on the ice crystal number concentration. *Atmospheric Chemistry and Physics*, **18 (19)**, 14 351–14 370.

Gryspeerdt, E., and Coauthors, 2020: Surprising similarities in model and observational aerosol radiative forcing estimates. *Atmospheric Chemistry and Physics*, **20 (1)**, 613–623.

Hawker, R. E., and Coauthors, 2021: The temperature dependence of ice-nucleating particle concentrations affects the radiative properties of tropical convective cloud systems. *Atmospheric Chemistry and Physics*, **21 (7)**, 5439–5461.

Held, I. M., and B. J. Soden, 2006: Robust responses of the hydrological cycle to global warming. *Journal of climate*, **19 (21)**, 5686–5699.

Hess, O., and R. Chemke, 2024: Anthropogenic forcings reverse a simulated multi-century naturally-forced northern hemisphere hadley cell intensification. *Nature Communications*, **15 (1)**, 4001.

Heyn, I., K. Block, J. Mülmenstädt, E. Gryspeerdt, P. Kühne, M. Salzmann, and J. Quaas, 2017: Assessment of simulated aerosol effective radiative forcings in the terrestrial spectrum. *Geophysical Research Letters*, **44 (2)**, 1001–1007.

Hoesly, R. M., and Coauthors, 2018: Historical (1750–2014) anthropogenic emissions of reactive gases and aerosols from the community emissions data system (ceds). *Geoscientific Model Development*, **11 (1)**, 369–408.

Hoose, C., and O. Möhler, 2012: Heterogeneous ice nucleation on atmospheric aerosols: a review of results from laboratory experiments. *Atmospheric Chemistry and Physics*, **12 (20)**, 9817–9854.

Johnson, B., J. Haywood, and M. Hawcroft, 2019: Are changes in atmospheric circulation important for black carbon aerosol impacts on clouds, precipitation, and radiation? *Journal of Geophysical Research: Atmospheres*, **124 (14)**, 7930–7950.

Kärcher, B., J. Hendricks, and U. Lohmann, 2006: Physically based parameterization of cirrus cloud formation for use in global atmospheric models. *Journal of Geophysical Research: Atmospheres*, **111 (D1)**.

Kärcher, B., and U. Lohmann, 2002: A parameterization of cirrus cloud formation: Homogeneous freezing of supercooled aerosols. *Journal of Geophysical Research: Atmospheres*, **107 (D2)**, AAC–4.

Kärcher, B., and U. Lohmann, 2003: A parameterization of cirrus cloud formation: Heterogeneous freezing. *Journal of Geophysical Research: Atmospheres*, **108 (D14)**.

Key, J. R., and A. J. Schweiger, 1998: Tools for atmospheric radiative transfer: Streamer and fluxnet. *Computers & Geosciences*, **24 (5)**, 443–451.

Khairoutdinov, M., and Y. Kogan, 2000: A new cloud physics parameterization in a large-eddy simulation model of marine stratocumulus. *Monthly weather review*, **128 (1)**, 229–243.

Koop, T., B. Luo, A. Tsias, and T. Peter, 2000: Water activity as the determinant for homogeneous ice nucleation in aqueous solutions. *Nature*, **406 (6796)**, 611–614.

Kooperman, G. J., M. S. Pritchard, S. J. Ghan, M. Wang, R. C. Somerville, and L. M. Russell, 2012: Constraining the influence of natural variability to improve estimates of global aerosol indirect effects in a nudged version of the community atmosphere model 5. *Journal of Geophysical Research: Atmospheres*, **117 (D23)**.

Koster, R. D., and Coauthors, 2015: Technical report series on global modeling and data assimilation, volume 43. Tech. rep., NASA-GMAO.

Larson, V. E., 2017: Clubb-silhs: A parameterization of subgrid variability in the atmosphere. *arXiv preprint arXiv:1711.03675*.

Liu, X., and J. E. Penner, 2005: Ice nucleation parameterization for global models. *Meteorologische Zeitschrift (Berlin)*, **14**.

Liu, X., J. E. Penner, S. J. Ghan, and M. Wang, 2007: Inclusion of ice microphysics in the ncar community atmospheric model version 3 (cam3). *Journal of Climate*, **20 (18)**, 4526–4547.

Loeb, N. G., and Coauthors, 2018: Clouds and the earth's radiant energy system (ceres) energy balanced and filled (ebaf) top-of-atmosphere (toa) edition-4.0 data product. *Journal of climate*, **31 (2)**, 895–918.

Lutsko, N. J., C. J. Wall, and B. Gasparini, 2026: An analytical model of the lifecycle of tropical anvil cloud radiative effects. *Journal of Geophysical Research: Atmospheres*, **131 (4)**, e2025JD045 070.

Lyu, K., X. Liu, J. Bacmeister, X. Zhao, L. Lin, Y. Shi, and O. Sourdeval, 2023: Orographic cirrus and its radiative forcing in ncar cam6. *Journal of Geophysical Research: Atmospheres*, **128 (10)**, e2022JD038 164.

Mitchell, D. L., A. Garnier, J. Pelon, and E. Erfani, 2018: Calipso (iir–caliop) retrievals of cirrus cloud ice-particle concentrations. *Atmospheric Chemistry and Physics*, **18 (23)**, 17 325–17 354.

NASA, 2025: Mcd06cosp_m3_modis – modis (aqua/terra) cloud properties level 3 monthly, 1x1 degree grid. Distributed Active Archive Center [data set], https://doi.org/10.5067/MODIS/MCD06COSP_M3_MODIS.062.

Neelin, J. D., and I. M. Held, 1987: Modeling tropical convergence based on the moist static energy budget. *Monthly Weather Review*, **115 (1)**, 3–12.

Nishant, N., S. C. Sherwood, and O. Geoffroy, 2019: Aerosol-induced modification of organised convection and top-of-atmosphere radiation. *npj Climate and Atmospheric Science*, **2 (1)**, 33.

Oshima, N., S. Yukimoto, M. Deushi, T. Koshiro, H. Kawai, T. Y. Tanaka, and K. Yoshida, 2020: Global and arctic effective radiative forcing of anthropogenic gases and aerosols in mri-esm2. 0. *Progress in Earth and Planetary Science*, **7 (1)**, 38.

Penner, J. E., Y. Chen, M. Wang, and X. Liu, 2009: Possible influence of anthropogenic aerosols on cirrus clouds and anthropogenic forcing. *Atmospheric Chemistry and Physics*, **9 (3)**, 879–896.

Penner, J. E., C. Zhou, A. Garnier, and D. L. Mitchell, 2018: Anthropogenic aerosol indirect effects in cirrus clouds. *Journal of Geophysical Research: Atmospheres*, **123 (20)**, 11–652.

Pierrehumbert, R. T., 1995: Thermostats, radiator fins, and the local runaway greenhouse. *Journal of the atmospheric sciences*, **52 (10)**, 1784–1806.

Pincus, R., P. A. Hubanks, S. Platnick, K. Meyer, R. E. Holz, D. Botambekov, and C. J. Wall, 2023: Updated observations of clouds by modis for global model assessment. *Earth System Science Data*, **15 (6)**, 2483–2497.

Regayre, L. A., and Coauthors, 2023: Identifying climate model structural inconsistencies allows for tight constraint of aerosol radiative forcing. *Atmospheric Chemistry and Physics*, **23 (15)**, 8749–8768.

Shi, X., X. Liu, and K. Zhang, 2015: Effects of pre-existing ice crystals on cirrus clouds and comparison between different ice nucleation parameterizations with the community atmosphere model (cam5). *Atmospheric Chemistry and Physics*, **15 (3)**, 1503–1520.

Smith, C. J., and Coauthors, 2020: Effective radiative forcing and adjustments in cmip6 models. *Atmospheric Chemistry and Physics*, **20 (16)**, 9591–9618.

Sokol, A. B., and D. L. Hartmann, 2022: Congestus mode invigoration by convective aggregation in simulations of radiative-convective equilibrium. *Journal of Advances in Modeling Earth Systems*, **14 (7)**, e2022MS003 045.

Sokol, A. B., C. J. Wall, and D. L. Hartmann, 2024: Greater climate sensitivity implied by anvil cloud thinning. *Nature Geoscience*, **17 (5)**, 398–403.

Sokol, A. B., and C. J. Wright, 2026: Sea surface temperature feedbacks and convective organization mediate the tropical circulation response to aerosols.

Song, C., and Coauthors, 2024: Buffering of aerosol-cloud adjustments by coupling between radiative susceptibility and precipitation efficiency. *Geophysical Research Letters*, **51 (11)**, e2024GL108 663.

Song, X., G. J. Zhang, C. Terai, and S. Xie, 2025: Enhanced convective microphysics scheme and its impacts on mean climate in e3sm. *Journal of Advances in Modeling Earth Systems*, **17 (5)**, e2024MS004 656.

Storelvmo, T., 2017: Aerosol effects on climate via mixed-phase and ice clouds. *Annual Review of Earth and Planetary Sciences*, **45 (1)**, 199–222.

Swales, D. J., R. Pincus, and A. Bodas-Salcedo, 2018: The cloud feedback model intercomparison project observational simulator package: Version 2. *Geoscientific Model Development*, **11 (1)**, 77–81.

Taylor, K., M. Crucifix, P. Braconnot, C. Hewitt, C. Doutriaux, A. Broccoli, J. Mitchell, and M. Webb, 2007: Estimating shortwave radiative forcing and response in climate models. *Journal of Climate*, **20 (11)**, 2530–2543.

Tully, C., D. Neubauer, N. Omanovic, and U. Lohmann, 2021: Cirrus cloud thinning using a more physically-based ice microphysics scheme in the echam-ham gcm. *Atmospheric Chemistry and Physics Discussions*, **2021**, 1–42.

Twomey, S., 1977: The influence of pollution on the shortwave albedo of clouds. *Journal of Atmospheric Sciences*, **34 (7)**, 1149–1152.

Twomey, S., 1991: Aerosols, clouds and radiation. *Atmospheric Environment. Part A. General Topics*, **25 (11)**, 2435–2442.

Virtanen, P., and Coauthors, 2020: SciPy 1.0: Fundamental Algorithms for Scientific Computing in Python. *Nature Methods*, **17**, 261–272, https://doi.org/10.1038/s41592-019-0686-2.

Vo, T., S. Po-Chedley, J. Boutte, J. Lee, and C. Zhang, 2024: xcdat: A python package for simple and robust analysis of climate data. *Journal of Open Source Software*, **9 (98)**, 6426.

Wall, C. J., T. Storelvmo, and A. Possner, 2023: Global observations of aerosol indirect effects from marine liquid clouds. *Atmospheric Chemistry and Physics*, **23 (20)**, 13 125–13 141.

Wall, C. J., and Coauthors, 2025: Decomposing cloud radiative feedbacks by cloud-top phase. *Journal of Climate*.

Watson-Parris, D., 2025: Integrating top-down energetic constraints with bottom-up process-based constraints for more accurate projections of future warming. *Geophysical Research Letters*, **52 (8)**, e2024GL114 269.

Weimer, M., C. Wilka, D. Kinnison, R. Garcia, J. Bacmeister, M. Alexander, A. Dörnbrack, and S. Solomon, 2023: A method for estimating global subgrid-scale orographic gravity-wave temperature perturbations in chemistry-climate models. *Journal of Advances in Modeling Earth Systems*, **15 (9)**, e2022MS003 505.

Williams, A. I., and N. Jeevanjee, 2025: A robust constraint on the response of convective mass fluxes to warming. *Journal of Advances in Modeling Earth Systems*, **17 (4)**, e2024MS004 695.

Wind, G., S. Platnick, M. D. King, P. A. Hubanks, M. J. Pavolonis, A. K. Heidinger, P. Yang, and B. A. Baum, 2010: Multilayer cloud detection with the modis near-infrared water vapor absorption band. *Journal of Applied Meteorology and Climatology*, **49 (11)**, 2315–2333.

Yamaguchi, T., R. Yoshida, Y.-S. Chen, I. L. McCoy, and G. Feingold, 2026: Dynamical and radiative influence on the hadley circulation by aerosol-cloud interactions. *Journal of Advances in Modeling Earth Systems*, **18 (4)**, e2025MS005 465.

Yook, S., S. Solomon, M. Weimer, D. E. Kinnison, R. Garcia, and K. Stone, 2025: Implementation of sub-grid scale temperature perturbations induced by non-orographic gravity waves in waccm6. *Journal of Advances in Modeling Earth Systems*, **17 (4)**, e2024MS004 625.

Zelinka, M., 2023: aprp. Zenodo [code], https://doi.org/10.5281/zenodo.5514141.

Zelinka, M. D., T. Andrews, P. M. Forster, and K. E. Taylor, 2014: Quantifying components of aerosol-cloud-radiation interactions in climate models. *Journal of Geophysical Research: Atmospheres*, **119 (12)**, 7599–7615.

Zelinka, M. D., L.-W. Chao, T. A. Myers, Y. Qin, and S. A. Klein, 2025: Recommendations for diagnosing cloud feedbacks and rapid cloud adjustments using cloud radiative kernels. *Atmospheric Chemistry and Physics*, **25 (3)**, 1477–1495.

Zelinka, M. D., S. A. Klein, and D. L. Hartmann, 2012: Computing and partitioning cloud feedbacks using cloud property histograms. part ii: Attribution to changes in cloud amount, altitude, and optical depth. *Journal of Climate*, **25 (11)**, 3736–3754.

Zelinka, M. D., C. J. Smith, Y. Qin, and K. E. Taylor, 2023: Comparison of methods to estimate aerosol effective radiative forcings in climate models. *Atmospheric Chemistry and Physics*, **23 (15)**, 8879–8898.

Zelinka, M. D., C. Zhou, and S. A. Klein, 2016: Insights from a refined decomposition of cloud feedbacks. *Geophysical Research Letters*, **43 (17)**, 9259–9269.

Zhang, G. J., and N. A. McFarlane, 1995: Sensitivity of climate simulations to the parameterization of cumulus convection in the canadian climate centre general circulation model. *Atmosphere-ocean*, **33 (3)**, 407–446.

Zhang, K., and Coauthors, 2014: On the use of nudging for aerosol–climate model intercomparison studies. *Atmospheric Chemistry and Physics*, **14 (16)**, 8631–8645.